BIONATURE 2017

The Eighth International Conference on Bioenvironment, Biodiversity and Renewable Energies

ISBN: 978-1-61208-561-6

ENVIROSENS 2017

The International Symposium on Remote Sensing for Climate and Earth Monitoring

May 21 - 25, 2017

Barcelona, Spain

BIONATURE 2017 Editors

Son V. Nghiem, Jet Propulsion Laboratory, California Institute of

Technology - Pasadena, USA

BIONATURE 2017

Foreword

The Eighth International Conference on Bioenvironment, Biodiversity and Renewable Energies (BIONATURE 2017), held between May 21 - 25, 2017 - Barcelona, Spain, covered these two main areas: environment and renewable and sustainable energies.

Environmental change awareness is a key state of spirit and legislation for preventing, protecting, and ultimately saving the planet biodiversity. Technical and practical methods for applying bio-agriculture for the public's health and safety are primary targets. The goal is the use of ecological economic stimuli in tandem with social and governmental actions preventing deforestation, pollution, and global warming. To cope with the climate and landscape changes advanced technical inventory of tools and statistics on lessons learned are needed to derive appropriate measure and plan accordingly.

Replacing the classical energy with alternative renewable energy (green energy), such as bioenergy, eolian energy, or solar energy is an ecological and economic trend that suggests important socio-economic advantages: using native renewable resources, increasing of self-sufficiency rate of energy and promoting use of clean energy, and that way, polluting emissions to the air will be reduced. Bioenergy is renewable energy derived from biological sources, to be used for heat, electricity, or vehicle fuel. Biofuel derived from plant materials is among the most rapidly growing renewable energy technologies. In several countries corn-based ethanol is currently the largest source of biofuel as a gasoline substitute or additive. Recent energy legislation mandates further growth of both corn-based and advanced biofuels from other sources. Growing biofuel demand has implications for U.S. and world agriculture. Eolian energy is currently used throughout the world on a large scale. In the past decade, its evolution shows its acceptance as a source of generation, with expressive growth trends in the energy matrices in the countries where this source is used Eolian energy is renewable and has very low environmental impact. To generate it, there are no gas emissions, no effluent refuse, and no other natural resources, such as water, are consumed. Photovoltaic technology makes use of the energy in the sun, and it has little impact on the environment. Photovoltaics can be used in a wide range of products, from small consumer items to large commercial solar electric systems. The event brought together the challenging technical and regulation aspects for supporting and producing renewable energy with less or no impact on the ecosystems. There are several technical integration barriers and steps for social adoption and governmental legislation to favor and encourage this kind of energy.

The BIONATURE 2017 conference also featured the following symposium:
- ENVIROSENS 2017 - The International Symposium on Remote Sensing for Climate and Earth Monitoring

We take here the opportunity to warmly thank all the members of the BIONATURE 2017 Technical Program Committee, as well as the numerous reviewers. The creation of such a high quality conference program would not have been possible without their involvement. We also kindly thank all the authors who dedicated much of their time and efforts to contribute to BIONATURE 2017. We truly believe that, thanks to all these efforts, the final conference program consisted of top quality contributions.

Also, this event could not have been a reality without the support of many individuals, organizations, and sponsors. We are grateful to the members of the BIONATURE 2017 organizing

committee for their help in handling the logistics and for their work to make this professional meeting a success.

We hope that BIONATURE 2017 was a successful international forum for the exchange of ideas and results between academia and industry and for the promotion of progress in the fields of bioenvironment and renewable energies.

We also hope that Barcelona provided a pleasant environment during the conference and everyone saved some time for exploring this beautiful city.

BIONATURE 2017 Chairs:

Suhkneung Pyo, Sungkyunkwan University - Suwon City, South Korea
Son V. Nghiem, Jet Propulsion Laboratory, California Institute of Technology - Pasadena, USA
Vladimir Strezov, Macquarie University - Sydney Australia
Silvia Paola Assini, University

BIONATURE 2017

Committee

BIONATURE Advisory Committee

Suhkneung Pyo, Sungkyunkwan University | School of Pharmacy, Republic of Korea
Son V. Nghiem, Jet Propulsion Laboratory, California Institute of Technology - Pasadena, USA
Vladimir Strezov, Macquarie University - Sydney, Australia
Silvia Paola Assini, University

BIONATURE 2017 Technical Program Committee

Silvia Paola Assini, University of Pavia, Italy
Yoseph Bar-Cohen, Jet Propulsion Lab (JPL), NASA
Benjamin Carbonnier, University Paris-East, France
Longjian Chen, China Agricultural University, China
Pedro Luiz Corrêa Pizzigatti is Escola Politécnica da USP (EPUSP), Brazil
Hany A. El-Shemy, Cairo University, Egypt
Valentinas Klevas, Lithuanian Energy Institute, Lithuania
Man-Kee Lam, Universiti Teknologi PETRONAS, Malaysia
Ana Jesús López Menéndez, Universidad de Oviedo, Spain
José Augusto Medrano Hernandez, Centro de Estudio de Tecnologías Energéticas Renovables (CETER) - CUJAE, Cuba
Son V. Nghiem, Jet Propulsion Laboratory, California Institute of Technology - Pasadena, USA
Suhkneung Pyo, Sungkyunkwan University | School of Pharmacy, Republic of Korea
Francisca Segura, University of Huelva, Spain
Vladimir Strezov, Macquarie University - Sydney, Australia

ENVIROSENS Advisory Committee

Martin Kappas, University of Göttingen, Germany
Shuanggen Jin, Shanghai Astronomcial Observatory, CAS, China

Program Committee Members

Thierry Badard, Centre for Research in Geomatics - Laval University, Quebec, Canada
Leandro Candido, EMBRAPA Instrumentação, Brazil
Aprile Cosimo, EPFL, Lausanne, Switzerland
Lucio André de Castro Jorge, Embrapa Instrumentation, Brazil
Gabriel de Oliveira, University of Kansas, USA
Fabio Del Frate, University of Rome Tor Vergata, Italy
Yongsheng Gao, Institute for Integrated Intelligent Systems | Griffith University, Australia
Garik Gutman, NASA, USA
Sergio Ilarri, University of Zaragoza, Spain
Shuanggen Jin, Shanghai Astronomcial Observatory, CAS, China
Michel Jourlin, Jean Monnet University, Saint-Etienne, France

Martin Kappas, University of Göttingen, Germany
Alexander Kokhanovsky, EUMETSAT, Germany

Copyright Information

For your reference, this is the text governing the copyright release for material published by IARIA.

The copyright release is a transfer of publication rights, which allows IARIA and its partners to drive the dissemination of the published material. This allows IARIA to give articles increased visibility via distribution, inclusion in libraries, and arrangements for submission to indexes.

I, the undersigned, declare that the article is original, and that I represent the authors of this article in the copyright release matters. If this work has been done as work-for-hire, I have obtained all necessary clearances to execute a copyright release. I hereby irrevocably transfer exclusive copyright for this material to IARIA. I give IARIA permission or reproduce the work in any media format such as, but not limited to, print, digital, or electronic. I give IARIA permission to distribute the materials without restriction to any institutions or individuals. I give IARIA permission to submit the work for inclusion in article repositories as IARIA sees fit.

I, the undersigned, declare that to the best of my knowledge, the article is does not contain libelous or otherwise unlawful contents or invading the right of privacy or infringing on a proprietary right.

Following the copyright release, any circulated version of the article must bear the copyright notice and any header and footer information that IARIA applies to the published article.

IARIA grants royalty-free permission to the authors to disseminate the work, under the above provisions, for any academic, commercial, or industrial use. IARIA grants royalty-free permission to any individuals or institutions to make the article available electronically, online, or in print.

IARIA acknowledges that rights to any algorithm, process, procedure, apparatus, or articles of manufacture remain with the authors and their employers.

I, the undersigned, understand that IARIA will not be liable, in contract, tort (including, without limitation, negligence), pre-contract or other representations (other than fraudulent misrepresentations) or otherwise in connection with the publication of my work.

Exception to the above is made for work-for-hire performed while employed by the government. In that case, copyright to the material remains with the said government. The rightful owners (authors and government entity) grant unlimited and unrestricted permission to IARIA, IARIA's contractors, and IARIA's partners to further distribute the work.

Table of Contents

From Millennium Development Goals to Sustainable Development Goals.
Are we on track?

Ana Jesús López Menéndez[1] and Rigoberto Pérez Suárez[1]

[1] Department of Applied Economics
School of Economics and Business
University of Oviedo
Campus del Cristo s/n 33006 Oviedo, Spain
e-mail: anaj@uniovi.es, rigo@uniovi.es

Abstract—In the framework of the 2030 Agenda for Sustainable Development, a list of 17 Sustainable Development Goals (SDG) has been approved connecting the issues of multidimensional poverty, inequality and exclusion, and sustainability. Seven of these goals are referred to environmental sustainability, thus significantly increasing the weight assigned to this field in the previous Millennium Development Goals (MDG). The monitoring of sustainable development goals represents a challenge, especially for less developed countries, where a data revolution is needed to address the existing gap. In spite of this fact, this paper provides significant evidence about the existing differences in the benefits of development between countries, suggesting the need of further efforts aimed at "*leaving no one behind*" as stated in the first SDG report.

Keywords- SDG; sustainability; poverty; environment; performance; convergence

I. INTRODUCTION

The challenge of ensuring environmental sustainability, already included in the list of Millenium Development Goals (MDG), is now more evident since the new Sustainable Development Goals connect the issues of multidimensional poverty, inequality and sustainability. More specifically, while MDG considered four different environmental targets, this number has significantly increased in the SDG, which contain seven environmental goals (numbers 7, 9, 11, 12, 13, 14, 15, as summarized in Table I), monitored though 77 indicators.

Furthermore, the Paris Agreement (United Nations [1]), entered into force on 4 November 2016, sets out a global action plan to avoid dangerous climate change by limiting global warming, thus strengthening efforts to achieve SDG, particularly goal number 13.

Within this context, this paper aims at monitoring the environmental MDG paying particular attention to the most vulnerable people and countries. In section 2 a performance index is computed for both environmental and poverty goals, while in section 3 we analyze the existing relationships, testing for convergence and country effects. Finally, section 4 provides some concluding remarks.

TABLE I. MDG AND SDG

Millennium Development Goals	Sustainable Development Goals
1- Eradicate extreme poverty and hunger	1-End poverty in all its forms everywhere 2-End hunger, achieve food security and improved nutrition and promote sustainable agriculture 3-Ensure healthy lives and promote well-being for all at all ages
2- Achieve universal primary education 3- Promote gender equality and empower women	4-Ensure inclusive and equitable quality education and promote lifelong learning opportunities for all 5-Achieve gender equality and empower all women and girls 8- Promote sustained, inclusive and sustainable economic growth, full and productive employment and decent work for all 10- Reduce inequality within and among countries
4- Reduce child mortality 5- Improve maternal health 6- Combat HIV/AIDS, malaria and other diseases	6- Ensure availability and sustainable management of water and sanitation for all
7- Ensure environmental sustainability	7- Ensure access to affordable, reliable, sustainable and modern energy for all 9- Build resilient infrastructure, promote inclusive and sustainable industrialization and foster innovation 11- Make cities and human settlements inclusive, safe, resilient and sustainable 12- Ensure sustainable consumption and production patterns 13- Take urgent action to combat climate change and its impacts 14- Conserve and sustainably use the oceans, seas and marine r resources for sustainable development 15- Protect, restore and promote sustainable use of terrestrial ecosystems, sustainably manage forests, combat desertification, and halt and reverse land degradation and halt biodiversity loss
8- Develop a global partnership for development	16- Promote peaceful and inclusive societies for sustainable development, provide access to justice for all and build effective, accountable and inclusive institutions at all levels 17- Strengthen the means of implementation and revitalize the global partnership for sustainable development

II. MONITORING ENVIRONMENTAL GOALS

Despite the lack of information for the less developed regions and some limitations in data coverage and quality, the SDG database and report [2] provide information for a wide variety of countries. More specifically, a panel has been considered including 135 countries and six different five-year periods referred to 1990, 1995, 2000, 2005, 2010 and 2015.

Regarding the monitoring framework, a report by the Sustainable Development Solutions Network [3] emphasizes the need of simplicity, high frequency and disaggregation and the UN Statistical Commission [4] agreed a list of SDG indicators, subject to refinements and improvements as methods and data availability improve. In this context, our analysis includes the proportion of population with access to electricity, the proportion of population with primary reliance on clean fuels and technology, the renewable energy share in the total final energy consumption, the emissions of Carbon Dioxide ($CO2$), the proportion of urban population living in slums and the material footprint per capita. Furthermore, since the elimination of poverty is a meaningful goal for development, the poverty rate has also been analyzed.

In order to monitor the evolution of these goals measuring the level of achievement of the proposed targets, two different indicators have been computed: the cumulative rate of growth and the performance index, given by the following expressions:

Cumulative rate of growth: $r = \left(\dfrac{X_t}{X_{1990}} \right)^{\frac{1}{t-1990}} - 1$

Performance index: $I_t = \dfrac{X_t - X_{1990}}{X_t * - X_{1990}}$

where $X_t, X_{1990}, X *$ respectively denote the current and initial values of the considered variables, and the specific target in the case that it exists.

A classification of countries can be established according to the obtained results in both environmental and poverty indicators, as collected in Table II. In general terms, countries behave satisfactorily, especially with regard to poverty, as it has been stressed in some recent reports [2], [5], [6]. However, some difficulties are found regarding environmental goals as the electricity access, the evolution of carbon dioxide emissions and the percentage of population living in slums.

Since the behaviour of the considered indicators varies widely across countries and the achievement of the sustainable development goals is particularly important for poor regions and countries, in the next sections we estimate econometric models with the aim of providing empirical evidence referred to the following questions:

-Does economic growth impact environmental SDG?
-Does convergence exist?
-Are there significant country and/or time effects?

TABLE II. CLASSIFICATION OF COUNTRIES ACCORDING TO ENVIRONMENTAL PERFORMANCE AND POVERTY REDUCTION

		Environmental Performance		
		Low	Medium	High
Poverty Reduction	High	Australia, Comoros, Niue, Virgin Islands,	Austria, Cyprus, Grenada, Israel, Japan, Kuwait, Netherlands, Norway, Reunion, Seychelles, Spain	Andorra, Belgium, Canada, Cook Islands, Czech Republic, Denmark, Finland, France, French Polynesia, Germany, Greenland, Guam, Iceland, Italy, Luxembourg, Micronesia, Monaco, Rep. Moldova, Singapore, Slovakia, Slovenia, Sweden, Switzerland, Macedonia, United Arab Emirates, United Kingdom, Yemen
	Medium	Algeria, Angola, Argentina, Bangladesh, Belize, Benin, Bolivia, Botswana, Brazil, Burkina Faso, Cambodia, Cameroon, Chad, Ecuador, Eritrea, Ethiopia, Ghana, Guatemala, Guinea, Haiti, Honduras, Indonesia, Kenya, Madagascar, Malawi, Malaysia, Maldives, Mali, Mexico, Mozambique, Namibia, Nepal, Pakistan, Panama, Paraguay, Peru, Senegal, Sierra Leone, Sri Lanka, Thailand, Togo, Trinidad Tobago, Uganda, Tanzania, Venezuela	Afghanistan, Bhutan, Burundi, Central African Republic, Chile, China, Colombia, Costa Rica, Dem Rep Congo, Dominican Republic, Egypt, Fiji, Greece, Guyana, India, Iran, Jamaica, Jordan, Kazakhstan, Kiribati, Libya, Mauritania, Morocco, Niger, Philippines, Portugal, Saint Lucia, Saudi Arabia, South Africa, Swaziland, Tonga, Tunisia, Turkey, Uruguay, Vietnam, Zambia	Aruba, Azerbaijan, Bahrain, Belarus, Bulgaria, Cote d'Ivoire, Croatia, Estonia, Hungary, Ireland, Kyrgyzstan, Lithuania, Romania, Rwanda, Serbia, Syria, United States, Uzbekistan
	Low	Antigua and Barbuda, Bosnia and Herzegovina, El Salvador, Georgia, Mauritius, Montserrat, Nicaragua, Nigeria, Papua N Guinea, Zimbawe	Barbados, Samoa	Marshall Islands, Palau, Puerto Rico, Russian Fed, Sudan, Tuvalu

Note: The classification of countries with regard to Environmental Performance and Poverty Reduction has been established according to the level accomplishment (%) of the corresponding targets: "High" if the level overcomes 75%, "Medium" for levels between 50% and 75% and "Low" otherwise.

III. CONVERGENCE ANALYSIS AND PANEL EFFECTS

In order to answer the previously proposed questions, we consider a panel database referred to 135 countries and 6 five-year periods from 1990 to 2015.

The convergence analysis has been performed for each environmental indicator, testing if the corresponding cumulative rate of growth is inversely related with the initial values. As summarized in Table III, although the goodness of fit (measured through the coefficient of determination) is quite poor, all the estimated coefficients show the expected negative sign.

Furthermore, the regression also includes the Gross Domestic Product (GDP) rate of growth, included in the MDG database, which appears to significantly affect the access to electricity (possitively) and the population living in slums (negatively).

TABLE III.   ENVIRONMENTAL SDG: CONVERGENCE ANALYSIS

Cumulative rate of growth of	Estimation results		
	Estimated coefficient of GDP Growth	*Estimated rate of convergence*	*R squared*
Proportion of population with access to electricity	0.47 (***)	-0.1 (***)	0.09
Proportion of population with primary reliance on clean fuels and technology	0	-0.01 (***)	0.32
Renewable energy share in the total final energy consumption	0,08	-0.03 (***)	0.17
Emissions of Carbon Dioxide (CO2)	-0,02	-0.27 (***)	0.10
Proportion of urban population living in slums	-0,17 (***)	-0.02 (***)	0.49
Material footprint per capita	0.03 (**)	-0.01 (***)	0.08

***significant at 1%; **significant at 5%; * significant at 10%

A more detailed analysis through panel estimation allows the identification of specific country and year effects. In this case, the dependent variable is the level of each environmental indicator and Table IV collects the main estimation results under the random effects hypothesis, which seems to be the most suitable option according to the Hausman test.

The empirical evidence confirms the impact of economic growth in the access of electricity and the population living in slums, thus confirming the previous results. Moreover, in this case, significant impact is also found over the emissions of carbon dioxide.

Given that this indicator has been identified as one of the main factors affecting the climate change, a more detailed analysis has been performed on carbon dioxide emission, whose econometric modeling and forecasting can be found in several works as Koirala et al [7], López et al [8], Pérez & López [9], among others. In general terms, these works confirm the need of new models of development and better environmental policies to avoid the costs of inaction both in economic and human terms.

TABLE IV.   PANEL ESTIMATION OF ENVIRONMENTAL SDG

Indicator	Estimation results	
	Estimated coefficient of GDP Growth	*Significant time effects*
Proportion of population with access to electricity	0.18 (***)	2000 (+) 2010 (+)
Proportion of population with primary reliance on clean fuels and technology	0.07	2005 (-) 2010 (-)
Renewable energy share in the total final energy consumption	-0.02	2000 (+)
Emissions of Carbon Dioxide (CO2)	0.004 (**)	2000 (+) 2005 (+)
Proportion of urban population living in slums	0.33 (*)	2000 (+) 2005 (+) 2010 (+)
Material footprint per capita	0.03	

***significant at 1%; **significant at 5%; * significant at 10%

According to the SDG panel database, CO2 emissions increase with economic growth and decrease as the share of renewable energy raises, thus confirming the findings of previous works [8] and emphasizing the need to promote broader energy access and increased use of renewable energy, as stated in SDG goal 7.

IV. CONCLUSION

In the framework of the Sustainable Development Goals, this paper provides empirical evidence about the evolution of environmental indicators.

More specifically, the analysis of a country database including SDG indicators confirms the existence of convergence, also detecting significant differences between countries.

These empirical findings suggest the need of fostering economic growth and the use of renewable energy in order to ensure access to affordable, reliable, sustainable and modern energy for all.

ACKNOWLEDGMENT

REFERENCES

[1] United Nations, Paris Agreement, United Nations Framework Convention on Climate Change, UNFCC, 2016.

[2] United Nations, The Sustainable Development Goal Report, New York, 2016.

[3] SDSN, Indicators and a Monitoring Framework for the Sustainable Development Goals Launching a data revolution for the SDGs, Secretary-General of the United Nations, Sustainable Development Solutions Network, 2015.

[4] United Nations, Report of the Inter-Agency and Expert Group on Sustainable Development Goal Indicators, Economic and Social Council, New York, March 2016.

[5] A. J. López and R. Pérez, "Green Growth and Sustainable Development. Monitoring Progress towards the Environmental Millennium Development Goals", BIONATURE 2013: The Fourth International Conference on Bioenvironment, Biodiversity and Renewable Energies, Lisbon, March 2013, pp. 21-24.

[6] A. J. López and R. Pérez, "Monitoring Sustainable Development: Lessons from MDG, Challenges for SDG".

European Conference on Quality in Official Statistics (Q2016), Madrid, May-June 2016, pp. 36-37.

[7] B.S. Koirala, H. Li, and R. P. Berrens, "Further Investigation of Environmental Kuznets Curve Studies using Meta-Analysis", Journal of Ecological Economics & Statistics, 22, 11, 2011, pp. 13-32.

[8] A. J. López, R. Pérez, and B. Moreno, "Environmental costs and renewable energy: Re-visiting the Environmental Kuznets Curve", Journal of Environmental Management, 145(1), 2014, pp. 368-373.

[9] R. Pérez and A. J. López, "Growing Green? Forecasting Environmental Indicators with Environmental Kuznets Curves and Logistic Growth Models", Environmental Science and Policy, 54, 2015, pp. 428-437.

Improving Downscaling Techniques for Glacier Studies Using Bio-Inspired Algorithms

Application to tropical glaciers in the Peruvian Andes

A.Tayebi, F. Álvarez-García, J. Gómez, F. Saez de
Adana, W. Cabos-Narváez

Group of Environmental and Climate Computing
Universidad de Alcalá
Alcalá de Henares, Spain
e-mail: hamid.tayebi@uah.es

M. Bonshoms

General Directorate of Meteorology
SENAMHI
Lima, Peru
e-mail: mbonshoms@senamhi.gob.pe

J. Úbeda

Group of High Mountain Physical Geography
Universidad Complutense de Madrid
Madrid, Spain
e-mail: joseubeda@ucm.es

Abstract— **This study aims at improving the performance of interpolation techniques applied to enhance the resolution of climatic information provided by regional models over glacierized areas, characterized by a complex topography and, most often, by the lack of sufficient observational coverage. Our proposal modifies previous methods in that it seeks to optimize the parameters of the vertical profile used to obtain interpolated temperature values on the surface at a given location attending to their agreement with directly interpolated values aloft over the same point. The optimization is achieved through the implementation of a Bio-Inspired Algorithm.**

Keywords- Downscaling; Bio-inspired algorithms; Climate Variability; Glaciers.

I. INTRODUCTION

The sensitivity of tropical glaciers to global climate change has been long noticed [1]. Their particular regime of ablation, essentially continuous throughout the year at their lowest altitude, leads to a fast response of their extent to modifications in their mass balance, hence to climate variations [2]. The Peruvian and Bolivian Andes harbor over 90% of these low-latitude ice packs, that represent a crucial water and energy resource for local as well as for downslope populations, including those in the extremely arid Pacific coast of South America [3][4]. The last thirty years have witnessed the retreat of tropical Andean glaciers at a pace without precedent in the past three centuries since the Little Ice Age maximum [5], posing severe socio-economic and ecological threats in the region. The urgent need for adaptation policies is, however, hampered by the multiple uncertainties that plague future projections of the evolution of the glacio-hydrological system. First and foremost, among the different causes of incertitude is the scarcity of observational records in these topographically complex areas. Regional Climate Models (RCMs) constitute a firm candidate to supply for this lack of climatic information. Their spatial resolution remains, however, low when confronted to the demands of glacio-hydrological studies, and the application of further downscaling techniques on the RCM data has already proven useful [6]. The inability of the RCM to capture the fine details on the surface, on account of its poor representation of the irregular relief and its associated steep gradients, advises against the direct downscaling of surface data, and the advantages of using upper air information for these mountainous regions has been recognized in a number of studies [7]–[10]. The present study follows this approach and attempts to implement an improvement on recent methodologies, based on the optimization of the agreement between directly interpolated upper-air temperatures over the targeted location and their estimation from the vertical lapse rates applied to obtain the surface values. The focus is on temperature over glacierized areas in the Peruvian Andes. The data employed in the analysis are described in detail in section II. Section III introduces the proposed methodology, and the contribution is closed with some final comments on the benefits expected from this technique.

II. DATA

The data to be downscaled in this study comes from a simulation with the atmospheric RCM REMO [11]. It is performed on two domains, with spatial resolution of 50 km and 25 km, respectively, driven at the boundaries by the ERA-Interim reanalysis [12], during the period 1980-2012. Both domains encompass the Peruvian Andes. The results of our downscaling procedure will be checked against observational records in the region provided by the Peruvian National Meteorological and Hydrological Service (SENAMHI).

III. METHODOLOGY

Our methodology is based on the technique described in [10], to which the reader is referred for a more detailed account. The vertical profile of temperature, up to the 500-hPa

level, at each of the four model grid points closest to the target location is fitted to a piecewise-linear function with two steps. Five parameters characterize this fit at each point: the upper and lower lapse rates, the corresponding intercepts (i.e., temperatures at sea level), and the height of the change point. In [10], these parameters are interpolated bilinearly and used to obtain the downscaled temperature at the point of interest. Here, the bilinear interpolation will be substituted by a weighted mean whose loadings are going to be determined in an optimization procedure. The temperature at the 500-hPa level over the target point is first estimated through a bilinear interpolation of the values at the model grid points. A second estimate of this mid-tropospheric temperature can be obtained from the local vertical profile of temperature, computed, as stated above, as a weighted mean of the profiles at the surrounding RCM grid points. The weights are sought to minimize the difference between the two estimates of the 500-hPa temperature over the target location. The procedure rests on the notion that the modeled upper-level temperature field is both smoother and closer to reality, and therefore should provide an adequate reference to aid in the determination of the local, downscaled, thermal profile.

In the last years, evolutionary computation algorithms, as genetic algorithms, evolution strategies and genetic programming have received a lot of attention with the objective of solving a wide range of non-linear optimization problems. Evolutionary algorithms are search methods inspired by natural evolution which adapt the environment changes to find an optimal solution to a problem through evolving a population of candidate solutions, during a generation based on the fitness values of each candidate and applying techniques of crossover, mutation and selection. Each type of evolutionary algorithm has its own specificities and that make them different one of each other.

The genetic algorithm that is going to be applied to optimize the parameters of the vertical profile used to obtain interpolated temperature values on the surface at a given location attending to their agreement with directly interpolated values aloft over the same point is shown next:

```
BEGIN
Generate initial population of individuals; // individual
is a feasible solution to a problem
Compute fitness of each individual; // higher fitness is
better solution
REPEAT // New generation
FOR population_size / 2 DO
Select two parents from old generation; // biased to the
fitter ones
Recombine parents for two offspring;
Mutate the offspring considering a certain probability
Compute fitness of offspring;
Insert offspring in new generation
END FOR
UNTIL population has converged
END
```

As can be seen, based on their fitness, parents are selected to reproduce offspring for a new generation. Fitter individuals have more chance to reproduce, whereas the old generation dies. The new generation has the same size as old generation. Offspring has a combination of the properties of two parents. If well designed, population will converge to an optimal solution.

REFERENCES

[1] S. Hastenrath, "Recession of tropical glaciers", Science, 265, pp. 1790–1791, 1994.

[2] L. G. Thompson, E. Mosley-Thompson, M. E. Davis, H. H. Brecher, "Tropical glaciers, recorders and indicators of climate change, are disappearing globally", Annals of Glaciology, 52(59), pp. 23–34, 2011.

[3] S. Rangecroft et al., "Climate change and water resources in arid mountains: an example from the Bolivian Andes", Ambio, 42(7), pp. 852–863, 2013.

[4] M. Vuille, "Climate change and water resources in the tropical Andes", Inter-American Development Bank, Technical note No. IDB-TN-515, 2013.

[5] A. Rabatel, et al, "Current state of glaciers in the tropical Andes: a multi-century perspective on glacier evolution and climate change", The Cryosphere, 7(1), pp. 81–102, 2013.

[6] M. Sharma, P. Coulibaly, Y. Dibike, "Assessing the need for downscaling RCM data for hydrologic impact study", Journal of Hydrologic Engineering, 16(6), pp. 534-539, 2010.

[7] Y. Durand, et al., "A meteorological estimation of relevant parameters for snow models", Annals of Glaciology, 18, pp. 65–71, 1993.

[8] L. A. Rasmussen and H. Conway, "Estimating South Cascade Glacier (Washington, U.S.A.) mass balance from a distant radiosonde and comparison with Blue Glacier", Journal of Glaciology, 47, pp. 579–588, 2001.

[9] L. A. Rasmussen and H. Conway, "Using upper-air conditions to estimate South Cascade Glacier (Washington, U.S.A.) summer balance", Journal of Glaciology, 49, pp. 456–462, 2003.

[10] A. H. Jarosch, F. S. Anslow, G. K. C. Clarke, "High-resolution precipitation and temperature downscaling for glacier models", 38 (1), pp. 391–409, 2012.

[11] D. Jacob and R. Podzun, "Sensitivity studies with the regional climate model REMO", Meteorology and Atmospheric Physics, 63(1), pp. 119–129, 1997.

[12] D. Dee et al., "The ERA‐Interim reanalysis: Configuration and performance of the data assimilation system", Quarterly Journal of the Royal Meteorological Society, 137(656), pp. 553–597, 2011.

Optimal Sizing of the ESS for Economic Advantage of PV-ESS Generation

Kyeong Hee Cho, Seul Ki Kim, Eung Sang Kim
Smart distribution research center
Korea Electro-technology Research Institute
Changwon-si, Republic of Korea
E-mail: kx1004xh@keri.re.kr

June Ho Park
Electronic engineering
Busan National University
Busan, Republic of Korea
E-mail: parkjh@pusan.ac.kr

Abstract—**Renewable energy Portfolio Standard (RPS) was implemented by the government of Republic of Korea. Public institutions have to install the renewable generator according to contract capacity. By mandatory systems like these, renewable energy market is consistently increasing. Photovoltaic power generation (PV) is affected by solar radiation and generate only during the day. If Energy Storage System (ESS) is connected to PV, surplus energy of PV is charged to ESS and ESS discharged to load in peak time period. In this paper, method of optimal sizing ESS for economic advantage for PV-ESS generation is suggested.**

Keywords- ESS sizing; PV-ESS; ESS Design; Economic analysis; Power pattern analysis.

I. INTRODUCTION

Renewable energy Portfolio Standard (RPS) was implemented by the government of Republic of Korea. The RPS system defines that power generation companies that have a 500MW or more of power generation facilities have to generate by renewable energy at a certain percentage of the total. Recently, if customer is public institution, this customer has to install the renewable generator more than 5 percentage of contracted capacity. By mandatory systems like these, market related to renewable energy is consistently increasing. In addition, on September 19, 2016, the Ministry of Trade, Industry and Energy (MOTIE) in Republic of Korea announced a policy to significantly expand the installation of Energy Storage System (ESS) in solar power plants. The purpose of the policy is that power of PV is affected by solar radiation and generated only during the day, so the ESS is connected to PV, surplus energy of PV is charged to ESS in the day and ESS can discharge to grid in peak time period.

The price of the ESS is about 622 [USD] per 1kW, which is very expensive compared to the electricity price. Economic damage may occur due to high investment costs of ESS when operator does not consider economic analysis for PV-ESS generation. Therefore, design is required before installing ESS and the market for ESS design to link PV is expected to expand significantly in Korea.

In this paper, we proposed a method of optimal sizing ESS for economic advantage of PV-ESS generation based on the experience of operating the ESS. Using the proposed method, operators who want to install ESS can reduce the economic risk of high investment cost of ESS and gain a maximum profit from linking PV and ESS.

In Section II, power pattern of PV is forecasted using local weather information. In Section III, the optimal scheduling algorithm of charging and discharging of ESS is explained. In Section IV, method of optimal sizing ESS for economic advantage for PV-ESS generation is proposed. In Section V, general economic analysis method is explained. In the case study from Section VI, ESS is designed for optimal ESS size selection using real solar radiation data. The paper is concluded with Section VII.

II. POWER PATTERN ANALYSIS OF PV

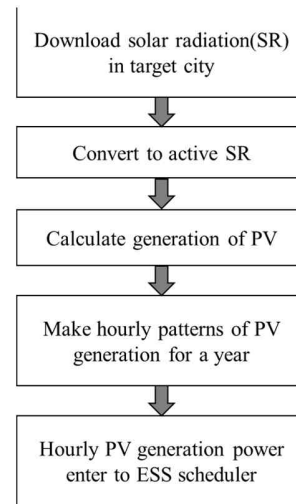The method for pattern analysis of PV is shown in Figure 1.

Figure 1. PV forecasting process

First of all, the data tables of Vertical Solar Radiation (VSR) in target city are downloaded. Then, VSR is converted to Active Solar Radiation (ASR) on the inclined surface of PV panel.

If $(90-\delta)$ is bigger than θ, then ASR is calculated following equation.

$$ASR = VSR / cos\theta \qquad (1)$$

Else if $(90-\delta)$ is smaller than θ, then ASR is calculated following equation.

$$ASR = VSR \times (\cos\theta + \sin\theta / \tan\delta) \qquad (2)$$

Where, VSR : Vertical Solar Radiation [kW]
ASR : Active Solar Radiation [kW]
θ: Angle of declination of PV panel
δ : Meridian altitude

Using hourly ASR data, PV generation is calculated using (3) [1].

$$P_{pv} = ASR \times C_{PV} \times \eta_{PCS} \qquad (3)$$

Where, P_{pv} : Power of PV system [kW]
C_{PV} : Capacity of PV [kW]
η_{PCS} : Efficiency of PCS [%]

The hourly PV generation pattern is made and entered into ESS scheduler.

III. OPTIMAL SCHEDULING OF ESS

When ESS is connected to PV, the process for optimizing the daily charging and discharging schedule of the ESS is explained in this section. In PV forecasted generation data, maximum hourly peak power value becomes rated output power of PCS.

A. Input data

Input information is a daily PV generation pattern for a year. Unit rate of electricity sales price and characteristics of ESS were entered as a unit price of System Marginal Price (SMP) and Renewable Energy Certificate (REC), available State of Charge (SOC), PCS efficiency and cycle efficiency.

B. Scheduling-charging

There are two constraints. First, the SOC of the battery is limited. The available capacity of battery is estimated by the following equation.

$$C_{BAT\_A} = C_{BAT} \times (SOC_{max} - SOC_{min}) \qquad (4)$$

Where, C_{BAT_A} : Available capacity of battery [kWh]
C_{BAT} : Capacity of battery [kWh]
SOC_{max}: Maximum of SOC [%]
SOC_{min} : Minimum of SOC [%]

Second, charging capacity of ESS at target hour i is calculated using the C_{BAT_A} and $P_{pv,t}$.
If $\sum_{t=1}^{i-1} P_{pv,t}$ is bigger than C_{BAT_A}, $P_{cha,i}$ is zero.
Else if $\sum_{t=1}^{i} P_{pv,t}$ is bigger than C_{BAT_A}, then $P_{cha,i}$ calculated following equation.

$$P_{cha,i} = C_{BAT\_A} - \sum_{t=1}^{i-1} P_{pv,t} \qquad (5)$$

Else, $P_{cha,i}$ calculated following equation.

$$P_{cha,i} = P_{pv,i} \qquad (6)$$

Where, $P_{pv,t}$: Power of PV according to hour t [kW]
$P_{cha,i}$: Charging power at target hour i [kW]
$P_{pv,i}$: Power of PV at target hour i [kW]
t : Time from 1 to 24 [hour]
i : Target hour [hour]

C. Scheduling-discharging

When PV generates electricity power from 6:00AM to 7:00PM, discharge of ESS is zero. The available capacity of battery (C_{BAT_A}) is equally divided in 10 hours from 8:00PM to 5:00AM. Then that amount is discharged. The reason for sharing discharging of ESS is that if the discharge duration is long, the efficiency is high. Table I is the efficiency table of lithium ion battery per discharging current.

TABLE I.   LITHIUM ION BATTERY EFFICIENCY PER DISCHARGING CURRENT

Discharge Duration [hour]	Discharge Current [C]	Efficiency [%]
5	0.2	100
1	1	99
0.2	5.2	98
0	10	95

IV. ECONOMIC ANALYSIS

Profit by generation is estimated using a unit price of SMP and REC.

SMP is calculated by adding $SM\,P_{PV}$ and $SM\,P_{ESS}$. Daily SMP profit equations is following.

$$SM\,P_{PV,d} = \sum_{t=1}^{24}\left(P_{pv,t} \times R_{SMP,unit,t}\right) \qquad (7)$$
$$SM\,P_{ESS,d} = \sum_{t=1}^{24}\left[(P_{dis,t} - P_{cha,t}) \times R_{SMP,unit,t}\right] \qquad (8)$$
$$SM\,P_{total\_month} = \sum_{d=1}^{30} SM\,P_{PV,d} + \sum_{d=1}^{30} SM\,P_{ESS,d} \qquad (9)$$
$$SM\,P_{total\_year} = \sum_{m=1}^{12} SM\,P_{total,m} \qquad (10)$$

Where, $SM\,P_{PV,d}$: SMP profit of PV at d day [USD]
$SM\,P_{ESS,d}$: SMP profit of ESS at d day [USD]
$SM\,P_{total\_month}$: Total SMP profit of ESS and PV during a target month [USD/month]
$SM\,P_{total\_year}$: Total SMP profit of ESS and PV during a target year [USD/year]
m : Target month
$R_{SMP,unit,t}$: SMP unit rate at hour t [USD]

REC is calculated by adding REC_{PV} and REC_{ESS}. Weight of PV is 1.5. When ESS discharged using SOC charged from PV generation, weight of ESS is 5.

$$REC_{PV,m} = \sum_{d=1}^{30}\left[\sum_{t=1}^{24}(P_{pv,t,d} - P_{cha,t,d})\right] \times R_{REC,unit,m} \times W_{PV} \qquad (11)$$
$$REC_{ESS,m} = \sum_{d=1}^{30}\left(\sum_{t=1}^{24} P_{dis,t,d}\right) \times R_{REC,unit,m} \times W_{ESS} \qquad (12)$$
$$REC_{total\_year} = \sum_{m=1}^{12}(REC_{PV,m} + REC_{ESS,m}) \qquad (13)$$

Where, $REC_{PV,m}$: REC profit of PV at m month [USD]

$P_{pv,t,d}$: Power of PV at hour(t) in a day(d) [kW]
$P_{cha,t,d}$: Charging power at hour(t) in a day(d) [kW]
$R_{REC,unt,m}$:REC unit rate at month m [USD]
W_{PV} : Weight of PV [REC]
$REC_{ESS,m}$: REC profit of ESS at m month [USD]
$P_{di,t,d}$: Discharging power at hour(t) in a day(d) [kW]
W_{ESS} : Weight of ESS link to PV [REC]
REC_{total_year} : Total REC profit of ESS and PV during a target year [USD/year]

$$\text{Total profits} = SM\,P_{total\_year} + REC_{total\_year} \quad (14)$$

Where, Total profits : Summation profits of SMP and REC for ESS and PV for a year [USD/year]

Profit is estimated and saved according to the capacity of ESS for 20 years. The profit is transposed to Net Present Value (NPV).

$$P_{NPV,after} = P_{NPV,before} \times (1-j)^n \quad (15)$$

Here, n : Period operating ESS [year]
$P_{NPV,after}$: Profit after NPV [USD]
$P_{NPV,before}$: Profit before NPV [USD]
j : Interest rate [%]

The unit price of PCS and battery is entered. Parameter is entered like as increasing rate of SMP, REC and money.
Using economic information, Internal Rate of Return (IRR) is estimated according to candidates of ESS.

$$0 = \sum_{t=0}^{19} \frac{CF_t}{(1+IRR)^t} \quad (16)$$

Here, CF_t : cash flow for each period t
t : xth year from target year

V. OPTIMAL SIZING OF ESS

Figure 2 presents the overall flow chart on economic analysis method for finding optimal ESS.

First, information on PV, ESS and price is entered. Using weather information in the target city, PV generation is forecasted. Initial and maximum capacity of ESS is selected and entered by the operator. ESS is scheduled for two cases (C_a, C_b) that are initial and maximum capacity. SMP and REC profit are estimated. Then economic analysis is calculated using PV and ESS cost.

If capacities of two cases are different ($|C_a - C_b| > 0$), another candidate (C_c) is selected as the center value between two cases. Then candidate (C_a) revised a capacity of better economic profit among the candidate capacities. And candidate (C_b) becomes candidate (C_c).

Two candidates are scheduled and calculated again. Iteration is performed until that difference of the two cases ($|C_a - C_b|$) is very small. This difference is set by the operator.

Optimal size ESS is selected among all candidates. We assume generally that the higher the IRR, the more economical it is.
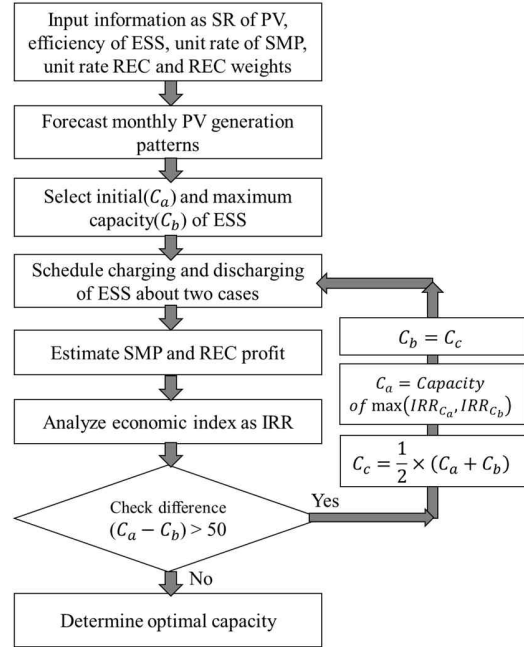

Figure 2. Flow chart of optimal ESS capacity estimation

VI. CASE STUDIES

In the case study, real SR data of Pusan city is downloaded from site of Korea meteorological administration [2]. Using Section II equation, PV power generation power is calculated monthly shown in Figure 3. PV capacity is 450 [kW] and fixed.

The angle of declination of PV panel is 50 [degree]. Meridian altitude is downloaded daily and inserted from the site of astronomy and space science information [3].
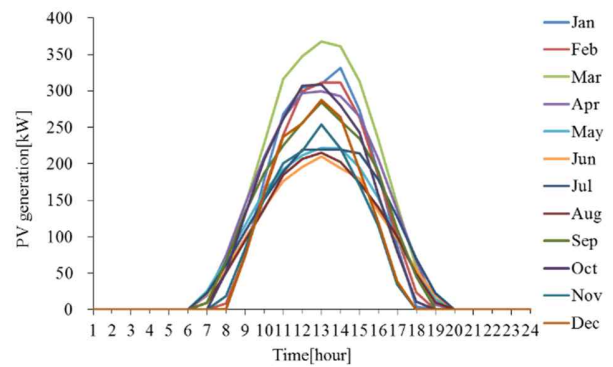

Figure 3. Monthly average pattern of PV forecast results

We assumed the boundary of battery capacity with the initial capacity is 100 [kWh] and maximum capacity is 800 [kWh]. The increasing unit capacity is 100 [kWh].

Rated output of PCS is selected to the maximum value of PV forecasted daily patterns for a year. But if this maximum

value is higher than battery capacity, rated output of PCS is battery capacity.

Determination of PCS rated output for each battery capacity is shown in Table II. As it can be seen, in Table II, PCS rated output does not increase linearly according to battery capacity. This means that the maximum value of PV forecasted daily patterns for a year is lower than the battery capacity starting from 700 [kWh]. Therefore maximum power of PCS is limited by 518 [kW].

TABLE II.　　DETERMINATION OF PCS RATED OUTPUT FOR EACH BATTERY CAPACITY

Cases	Capacity		
	PV[kW]	Battery[kWh]	PCS rated output[kW]
1	450	100	80
2	450	200	136
3	450	300	212
4	450	400	292
5	450	500	372
6	450	600	452
7	450	700	518
8	450	800	518

In the case study, the average of SMP unit rate is about 0.12 [USD/kW] and the average of REC unit rate is about 70.13 [USD/MW].

The profits of SMP and REC for cases of Table II were calculated using equations (7)-(14). SMP profit of ESS and PV during a target month and year were calculated using equation (10) (see Table III). The total REC profit of ESS and PV during a target year were calculated using equation (13) (see Table III). The summation profits of SMP and REC for ESS and PV for a year were calculated using equation (14) as can be seen in Table III. The results of Table III show the accumulated profits for 20 years.

TABLE III.　　PROFITS ESTIMATION RESULTS FOR EACH CASE

Cases	PV profit [USD]		ESS profit [USD]		Total Profit [USD]
	$SM\ P_{PV}$	REC_{PV}	$SM\ P_{ESS}$	REC_{ESS}	
1	58,966	52,294	2,801	13,145	127,206
2	55,768	49,402	5,574	26,159	136,903
3	52,590	46,536	8,320	39,056	146,502
4	49,477	43,732	11,006	51,672	155,888
5	46,442	41,002	13,627	63,956	165,027
6	43,490	38,359	16,175	75,854	173,877
7	40,602	35,784	18,665	87,437	182,488
8	37,770	33,264	21,106	98,781	190,920

Using equations (15) and (16), economic analysis results of these cases are shown in Table IV. The NPV of profit has been calculated using equation (15) (see Table IV). The IRR has been calculated using equation (16) as can be seen in Table IV. The accumulated profits during 20 years are presented in Table IV.

The cost of PV and ESS per unit like Table V was inserted to simulation.

TABLE IV.　　ECONOMIC ANALYSIS RESULTS FOR EACH CASE

Cases	Cost of PV and ESS [USD]	IRR [%]	(Profit-Cost) [USD]	Payback [year]
1	902,972	8.23	713,638	8.79
2	965,599	8.34	774,577	8.72
3	1,038,151	8.26	823,782	8.77
4	1,110,704	8.17	870,195	8.83
5	1,183,256	8.07	913,383	8.90
6	1,241,941	8.13	967,385	8.85
7	1,285,647	8.36	1,034,039	8.71
8	1,329,354	8.55	1,098,357	8.58

TABLE V.　　UNIT COST OF EACH PV, BATTERY AND PCS

Equipment	Unit	Cost[USD]
PV system	1kW	1,594
Battery of Lithium ion	1kWh	354
PCS	1kW	221
Construction cost	1kW	89

Graph of IRR, PV profit and ESS profit for each case in Table IV are shown in Figure 4. As shown in Figure 4, the IRR was lowest when ESS and PV profits were equal.
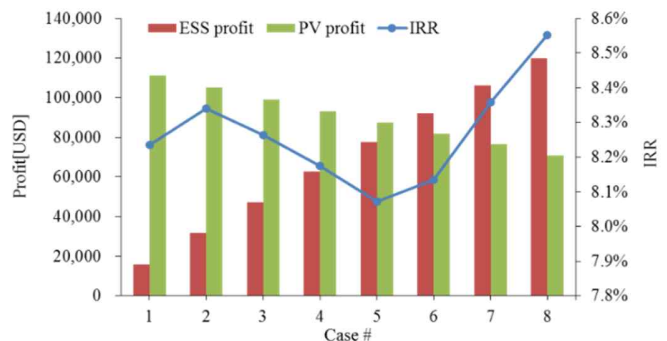

Figure 4.　The IRR graph according to battery capacity candidates

In order to apply the algorithm presented in Figure 2, information is entered and PV generation is forecasted. The initial capacity was set at 200 [kWh] and the maximum capacity was set at 3,000 [kWh]. The ESS of two cases was scheduled respectively and their profits were calculated. Also, economy analysis is calculated. Capacity difference of two cases is checked. If this difference is smaller than 50 [kWh], simulation is terminated. If not, simulation is repeated. One capacity among next two cases is center capacity of previous candidates. Another capacity is the capacity of previous candidates with the largest IRR. For example, in the second simulation, previous candidate (C_a) is 200 [kWh], previous candidate (C_b) is 3,000 [kWh]. Therefore candidate (C_c) is 1,600 [kWh], next candidate (C_a) is 200 [kWh] and next candidate (C_b) is 1,600 [kWh].

TABLE VI.   DETERMINATION OF BATTERY CAPACITY BY FIGURE 2 AND IRR RESULTS

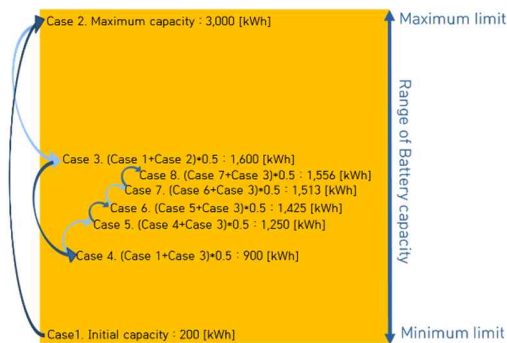| Cases	Battery capacity[kWh]	IRR[%]
1	200	8.34
2	3,000	7.17
3	1,600	9.33
4	900	8.71
5	1,250	9.14
6	1,425	9.26
7	1,512.5	9.30
8	1,556.3	9.32

Figure 5.   Selection of battery capacity for increasing IRR by Figure 2
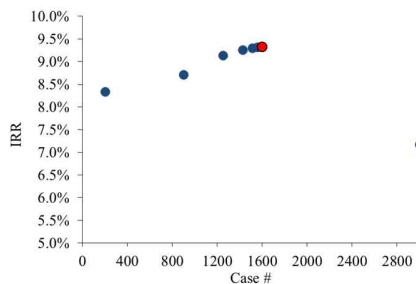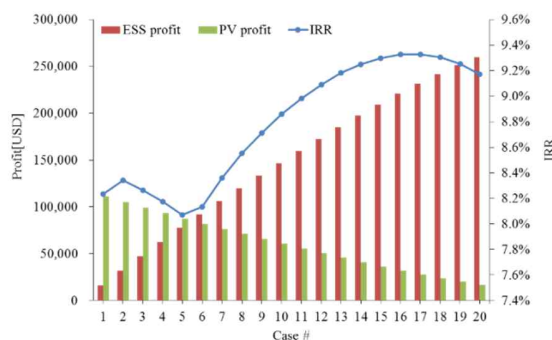

Figure 6.   IRR curve according to each case

Figure 7.   IRR curve while increasing battery capacity by 100

As it can be seen in Figure 5, optimal size, which is 1,600 [kWh], was found by running simulation 8 times. This case depends on the assumed conditions.

In this case study, full combination means all cases of battery capacity increasing by same term from minimum to maximum. Full combination had simulated capacity cases to increase by 100 [kWh] up to 2,000 [kWh]. We depicted the curve of Profits and IRR in Figure 6.

When the battery capacity increasing by 100 [kWh] is simulated, the IRR curve changes as parabolic curve. This method requires 20 iteration and shows that optimal battery size is 1,600 [kWh].

VII.   CONCLUSION

In this paper, the method of optimal sizing of the ESS for the economic advantage of PV-ESS generation was proposed. The economic advantage included generation profits of SMP and REC considering REC weight of discharging power of ESS charged from PV.

In the case study, in order to apply the algorithm presented in Figure 2, ESS capacities were selected and scheduled. The generation profits and IRR of each case were calculated for optimal ESS size selection. The simulation repeated until that the difference of capacities was smaller than 50 [kWh]. In the results, the optimal size, which was 1,600 [kWh], was found by running simulation 8 times. For comparison, full combination had simulated all capacity cases to increase by 100 [kWh] up to 2,000 [kWh]. This method requires 20 iteration. Optimal battery size of full combination was 1,600 [kWh]. Since the results were the same, showing that the method applied was accurate and faster.

Using the proposed method, operators who want to install ESS can select the optimal capacity that maximize the profit by linking PV and ESS for generation business. Future work will be focused on comparisons of optimal sizing method of the ESS according to two different goals of demand management and generation business.

REFERENCES

[1] Md. Habibur Rahman and S. Yamashiro, "Novel Distributed Power Generating System of PV-ECaSS Using Solar Energy Estimation", IEEE Transactions on energy converstion, Vol. 22, No. 2, pp.360, June 2007.

[2] Korea meteorological administration site, http://web.kma.go.kr/eng/index.jsp, April, 2017.

[3] Astronomy & space science information site, http://astro.kasi.re.kr/main/mainpage.aspx, April, 2017.

[4] K. H. Cho, S. K. Kim, and E. S. Kim, "Optimal Capacity Determination Method of Battery Energy Storage System for Demand Management of Electricity Customer", Transactions of the Korea Institute of Electrical Engineers, Vol. 62, No.1, pp. 21–28, January, 2013

[5] K. H. Cho, S. K. Kim, and E. S. Kim, "Optimal Sizing of BESS for Customer Demand Management", Journal of ICEE, Vol.1, January, 2014.

One Day Ahead Forecasting of Generating Power for Photovoltaic Power System

Hyang-A Park
Smart Distribution Research Center
Korea Electrotechnology Research Institute
Changwon-si, Republic of Korea
e-mail : giddk100414@keri.re.kr

Jong-yul Kim
Smart Distribution Research Center
Korea Electrotechnology Research Institute
Changwon-si, Republic of Korea
e-mail : jykim@keri.re.kr

Eung-Sang Kim
Smart Distribution Research Center
Korea Electrotechnology Research Institute
Changwon-si, Republic of Korea
e-mail : eskim@keri.re.kr

Sung-shin Kim
Department of Electrical and Computer Engineering
Pusan National University
Busan, Republic of Korea
e-mail : sskim@pnu.ac.kr

Abstract—**Photovoltaic power generation is affected much by weather and temperature, so the amount of power generation is not constant and there are many difficulties in predicting. Thus, the accurate prediction of the photovoltaic power due to climate change is critical to stable electricity supply. In this paper, in order to create a power generation forecast model, the data, such as power generation, temperature, Daily Mean Cloud Amount (DMCA) data has been collected from April 2016 to September 2016. Using the neural network, the peak solar irradiation forecasting model was created, solar irradiation was calculated from the peak solar irradiation predicted, and finally the model to predict power generation was made. In this paper, the peak solar irradiation is predicted using the maximum temperature and the peak solar irradiation data, and ultimately the solar power generation is predicted through the predicted peak solar irradiation.**

Keywords - Solar irradiation; Neural network; Photovoltaic; Forecasting model.

I.   INTRODUCTION

Recently, concern for the development of alternative energy resources has been growing as the energy problem gets worse worldwide. Accordingly, the importance of renewable energy is emerging and the proportion of photovoltaic (PV) power system in the various renewable energy sources is increasing. Nowadays the use of the distributed power generating systems, especially those using PV, is increasing due to the maintenance free, long lasting, and environment friendly nature of PV [1]. Accurate prediction of PV generation accompanying climate change is important for stable supply of electric power, since PV generation is most sensitive to climate change among renewable energy sources.

In this paper, the data measured by the energy Management System (EMS) built in the smart grid system is utilized, and the prediction of the PV power generation aims at the efficient energy management of the EMS. In Section II, past temperature data and solar irradiation data were collected and analyzed, and the maximum temperature and the peak solar irradiation were classified. In Section III, peak solar irradiation was predicted using the Neural Network (NN). Utilizing the predicted peak solar irradiation, finally, the amount of PV power generation was predicted.

II.   ANALYSIS OF EXPERIMENTAL DATA

First of all, before starting the experiment, temperature data, solar irradiation data and DMCA data from April 2016 to September 2016 were collected and analyzed. Daily maximum temperature and daily peak solar irradiation data were calculated and classified. Temperature and DMCA data were collected from the Meteorological Agency and solar irradiation data was collected through its own EMS. Figure 1 shows the experimental data of hourly solar irradiation during April - September 2016. The DMCA data, peak irradiation data, and maximum temperature data were normalized, and the correlation of the normalized data was analyzed. Figure 2 shows the relationship between peak solar irradiation and DMCA data. As a result of analyzing the normalized DMCA and normalized maximum solar irradiation, it can be confirmed that nonlinear inverse proportional curves are created in which the solar irradiation becomes smaller and smaller as the DMCA is larger. Here, the normalized DMCA value 0 means sunny, 1 means very cloudy. Figure 3 shows relationship between peak solar irradiation and maximum temperature. The maximum temperature and the peak solar irradiation are also normalized and then analyzed. As a result, as for the maximum temperature and peak solar irradiation, a nonlinear proportional curve is created as shown in Figure 3 and was predicted. Using the analyzed data, a peak solar irradiation prediction model is created, and the peak solar irradiation is predicted by this forecasting model. Then, the daily solar irradiation was predicted from the predicted peak solar irradiation, and finally the amount of PV power generation.
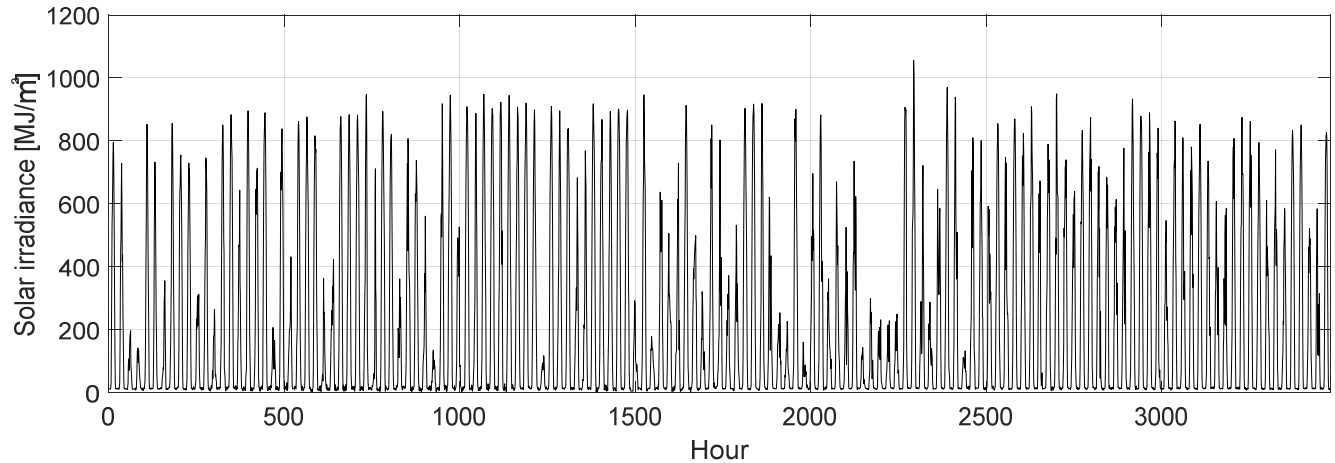
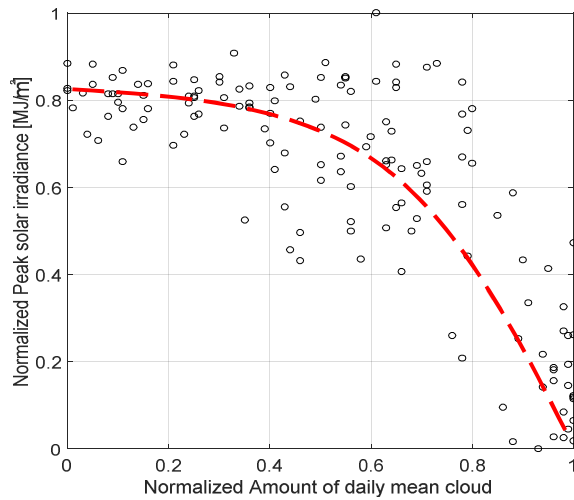Figure 1.   Experimental data of hourly solar irradiation

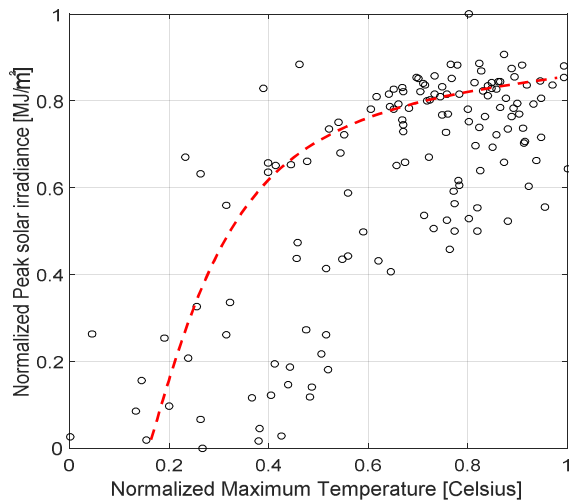Figure 2.   Relationship between peak solar irradiation and daily mean cloud amount data

Figure 3.   Relationship between peak solar irradiation and maximum

III.   SIMULATION

In this paper, simulation to predict one day ahead generating power output for PV system was executed for efficient energy management of EMS. In order to compare the actual generating power amount of the PV power generation system with the predicted PV output value of the program, the research institution of City C in Korea is selected and installed, and the capacity of the PV system is 50 kW.

Single layer feedforward NN [2] was used for peak solar radiation forecasting algorithm. NN is very effective in prediction and is used in various fields, and the model output value calculated by input and the desired output value update the connection weight to minimize the error. The input layer receives as parameters the peak solar irradiation, the maximum temperature and the DMCA, while the output layer gives as parameters the peak solar irradiation at the next day [3]. Prior to performing the algorithm, DMCA data, maximum temperature data, peak solar radiation amount data as the input data are normalized between 0 and 1. The simulation was carried out assuming that tomorrow's cloud data and maximum temperature data are known through the Meteorological Agency forecasts. Peak solar irradiation was predicted by using single layer feedforward NN with maximum temperature, peak solar irradiation, DMCA as input data. The generating power for PV system was calculated by using the least squares method, which is a method for minimizing the sum of squares of distances between actual values and values predicted by trend lines.

IV.   FORECASTING RESULT OF POWER OUTPUT

Figure 4 shows the forecasting of daily peak solar irradiation and the solar irradiation. The solar irradiation that has not been measured was excluded from the simulation in September 2016. Figure 5 shows the chart of predicted solar irradiation for sunny day and Figure 6 shows the chart of predicted solar irradiation for cloudy day.
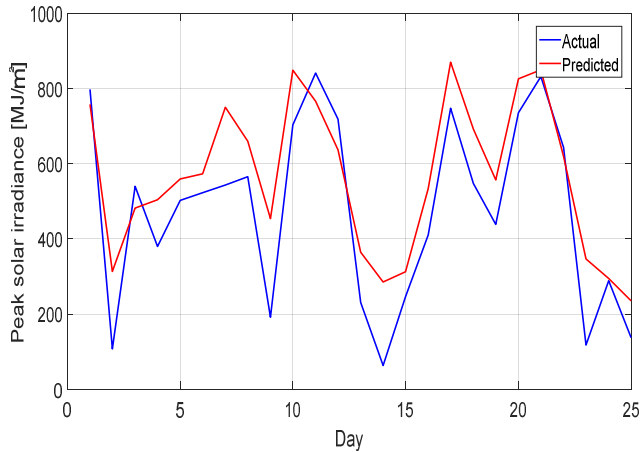
Figure 4.   Forecasting of daily peak solar irradiation in September 2016
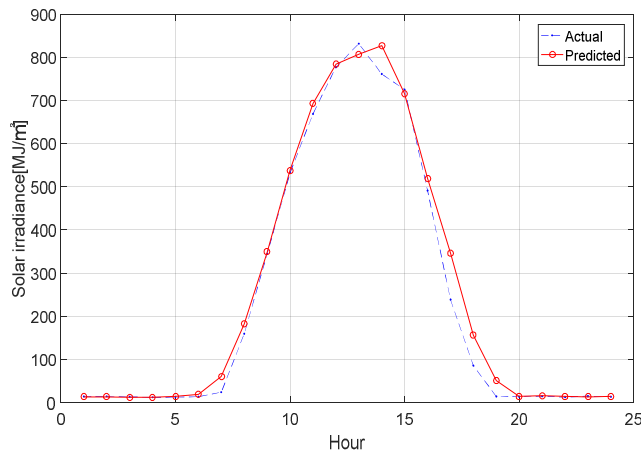

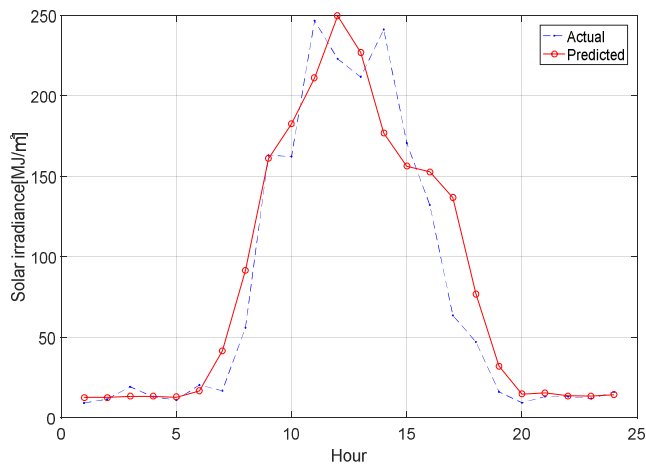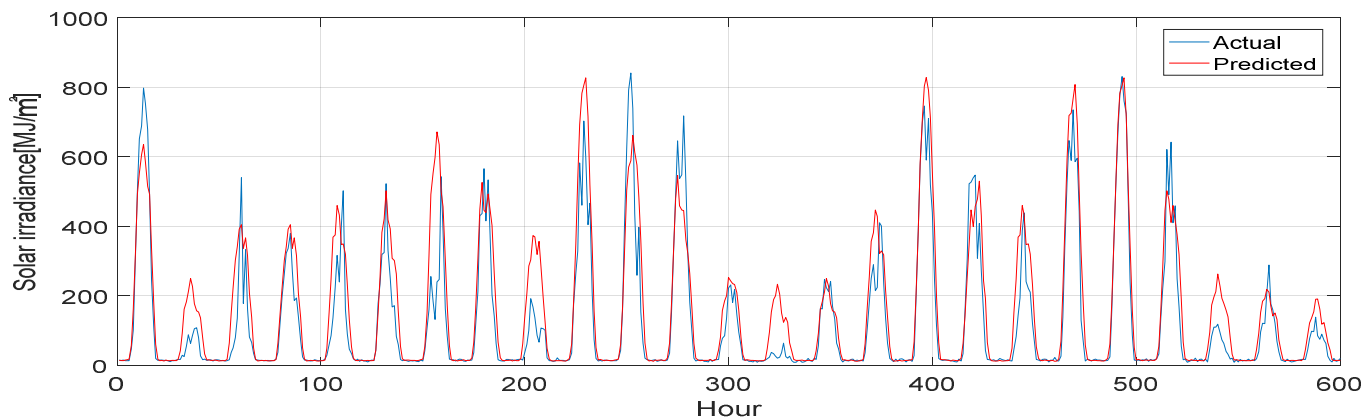Figure 5.   Forecasting of solar irradiation for sunny day

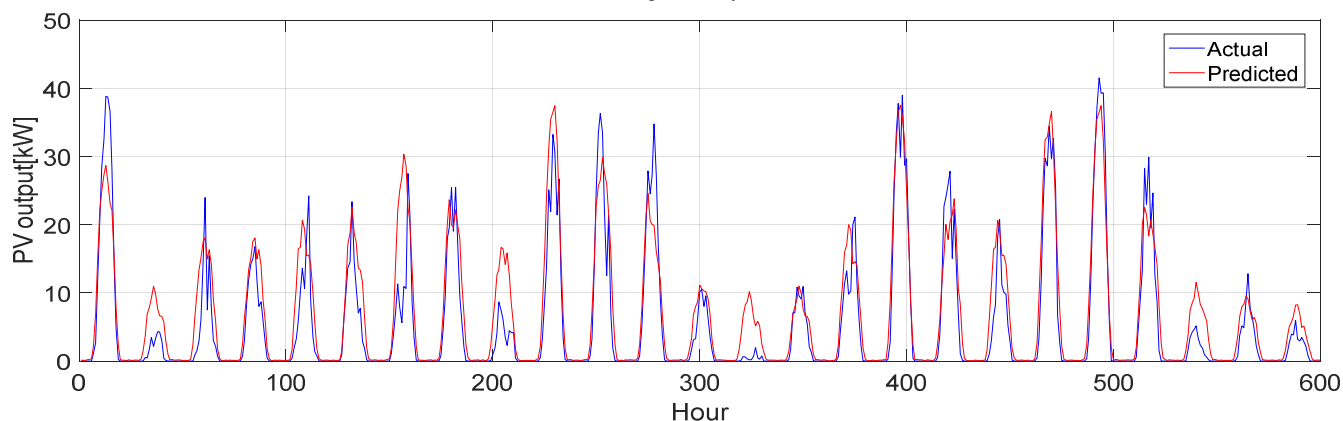Figure 6.   Forecasting of solar irradiation for cloudy day

TABLE I.   DAILY SOLAR IRRADIANCE

Hour	Cloudy day(9/18)		Sunny day(9/24)	
	Actual data [MJ/m^2]	Predicted data [MJ/m^2]	Actual data [MJ/m^2]	Predicted data [MJ/m^2]
1	9.3	12.8	14.3	13.1
2	11.6	12.8	14.7	13.1
3	19.4	13.5	13.4	12.3
4	13.2	13.5	12.4	12.3
5	11.1	12.9	12.7	14.4
6	20.5	16.8	13.6	19.3
7	16.9	41.8	24.2	60.4
8	56.0	91.7	159.6	182.3
9	163.1	161.1	344.4	349.0
10	162.3	182.8	532.4	538.1
11	246.7	211.2	668.8	692.6
12	223.0	249.7	776.9	783.8
13	221.8	227.0	831.4	806.7
14	241.2	176.9	761.1	827.2
15	170.7	156.3	725.1	715.9
16	132.2	152.8	491.2	519.1
17	63.7	136.7	238.6	346.2
18	47.2	77.1	85.7	156.3
19	16.2	32.3	14.4	50.6
20	9.4	14.8	13.6	14.3
21	13.3	15.6	14.9	16.1
22	13.3	13.7	12.7	14.7
23	12.1	13.5	15.1	13.3
24	16.1	14.5	13.5	14.3

Table 1 shows a comparison of Actual solar irradiance data and predicted solar irradiance data. Through Table 1, it is possible to confirm that predicted solar irradiance and the accuracy of the prediction were verified with Mean Absolute Percentage Error (MAPE). As a result of obtaining the MAPE of the forecasted solar irradiation from 10 a.m. to 4 p.m. when the amount of sunlight increased, MAPE was 3.2% on a sunny day and MAPE was 12.3% on a cloudy day. It is difficult to predict because the shape, quantity and weight of the cloud cannot be confirmed and clouds are a major contributor to the amount of solar radiation. Through Figure 5 and Figure 6, it can be confirmed that the hourly solar irradiation on a sunny day is comparatively better than the day with clouds. Figure 7 shows a comparison between actual data and predicted data. Figure 7(a) shows forecasting of hourly solar irradiation and Figure 7(b) show forecasting of hourly generating power output for PV system in September in 2016.

(a)   Forecasting of hourly solar irradiation

(b)   Forecasting of hourly generating power output for PV system

Figure 7.   Comparison of Actual data and Predicted data

It can be confirmed by seeing Figure 7 that the hourly solar irradiation curve pattern and the hourly generating power output of for PV system curve pattern are similar.

V.   CONCLUSION

This study predicted PV power generation to make a plan for operating ESS efficiently. In Section II, temperature, solar irradiation and DMCA data from April 2016 to September 2016 were collected and analyzed. In Section III, by using NN, the peak solar irradiation amount was predicted, and one day ahead daily solar irradiation amount was also predicted using the predicted peak solar irradiation amount. Then, PV power generation amount was predicted using the predicted daily solar irradiation amount. Experimental comparison between generating power output forecasted through experiments and actual PV output data and predicted solar irradiation amount and actual solar irradiation data were compared. The proposed method shows that the predicted PV values and the actual PV values are displayed in a similar curve pattern. The forecast of PV on a sunny day improved relatively, but in the case of many clouds, the accuracy of the forecast of PV decreased due to the amount of clouds and various factors. For follow-up research, solar altitude data will be added to the input data of the solar prediction model.

REFERENCES

[1]   M. H. Rahman and S. Yamashiro. "Novel distributed power generating system of PV-ECaSS using solar energy estimation." IEEE Transactions on Energy Conversion, vol. 22(2), pp.358-367, 2007.

[2]   A. Yona, T. Senjyu, A. Y. Saber, T. Funabashi, H. Sekine and C. H. Kim. "Application of neural network to one-day-ahead 24 hours generating power forecasting for photovoltaic system." Intelligent Systems Applications to Power Systems, 2007. ISAP 2007. International Conference on. IEEE, pp.1-6, 2007.

[3]   A. Mellit and A. M. Pavan. "A 24-h forecast of solar irradiance using artificial neural network: Application for performance prediction of a grid-connected PV plant at Trieste, Italy." Solar Energy,   vol.84(5), pp.807-821, 2010

The Antarctic Circumpolar Frontal Ice Zone

S. V. Nghiem, G. Neumann, and D. T. Nguyen
Jet Propulsion Laboratory
California Institute of Technology
Pasadena, California, U.S.A.
e-mail: Son.V.Nghiem@jpl.nasa.gov

A. Moreira and I. Hajnsek
German Aerospace Center
Microwaves and Radar Institute
Oberpfaffenhofen, Germany
e-mail: Alberto.Moreira@dlr.de

Abstract—**Antarctic and Arctic sea ice characteristics are starkly contrasted. Antarctic sea ice is encapsulated by a frontal ice zone (FIZ), which is a circumpolar band of sea ice consisting of older and thicker ice adjacent to the ice edge, while Arctic sea ice contains younger and thinner ice in the marginal ice zone along the ice edge. Here we examine the distribution and properties of the FIZ using NASA remote sensing data from a satellite scatterometer and from Operation IceBridge. Results show that the FIZ is a persistent feature, where sea ice is continually built up by a supply of younger sea ice effectively produced and transported from the internal ice pack. During the ice growth season, the FIZ becomes rougher, due to ice deformation and ridging, and thereby thicker. Also sustained by westerly winds and currents, the FIZ supports the maintenance of the ice cover. Future coordinated campaigns with surface and aircraft observations, together with high-resolution multi-dimensional measurements by the TanDEM-X satellite polarimetric and interferometric radar, are crucial to characterize, understand, and predict Antarctic sea ice change.**

Keywords-Antarctic sea ice; frontal ice zone; remote sensing; satellite scatterometer; Operation IceBridge; TanDEM-X SAR.

I. INTRODUCTION

The total extent of Antarctic sea ice has been preserved and even slightly increased in contrast to the drastic decrease of Arctic sea ice in recent decades. The opposite behavior in the interdecadal change of Antarctic and Arctic sea ice is considered by scientists as a paradox [1]-[4], which the cryospheric science research community has been struggling to explain. The stratospheric ozone depletion was suggested to cause atmospheric change that would maintain Antarctic sea ice [5][6]; however, this explanation was challenged by Sigmond and Fyfe [7]. Others relied on fresh meltwater and salinity reduction [8][9] and on wind effects [10][11] to address the paradox while leaving several issues unresolved.

For an explanation of the polar sea ice paradox to be plausible, it requires self-consistent answers simultaneously to all of these science questions about Antarctic sea ice: (1) What are the most effective processes for sea ice production pertaining to Antarctic conditions? (2) What are the factors protecting the sea ice cover? (3) What are the factors sustaining sea ice? (4) What are the factors causing regional variability? (5) Is there any discord among these factors? (6) Why do opposite effects occur in Antarctic and Arctic sea ice while both have to obey the same physics?

In a recent publication [12] using satellite and surface observations to address the above science questions, Nghiem et al. have presented an original research that 'gives a plausible explanation for the difference in the Arctic and Antarctic sea ice response to the climate change of recent decades' as noted by the peer review. A key finding is the formation of a formidable circumpolar FIZ that shields and thereby protects the internal younger and thinner sea ice.

Here we further examine the characteristics of the FIZ in the Southern Ocean encircling Antarctica. Remote sensing data used in this study include both satellite and aircraft data. In Section II, we present results from radar backscatter data, collected by the SeaWinds scatterometer aboard the QuikSCAT satellite (QS) in 1999-2009. Section III shows observations from aircraft acquired during the NASA's Operation IceBridge (OiB) in 2009 together with the satellite results. Section IV highlights the characteristics of the FIZ in sustaining Antarctic sea ice, and presents a concept for future Antarctic field campaigns with coordinated surface, aircraft, and satellite observations, including TanDEM-X synthetic aperture radar (SAR), to advance sea ice science. The last section provides the summary and conclusion.

II. SATELLITE OBSERVATIONS

The immense extent of Antarctic sea ice requires satellite observations such as QS to identify and map different sea ice classes with different physical characteristics. QS was launched from the space complex at Vandenberg Air Force Base, California, in June 1999. QS radar backscatter data were acquired globally across orbit swaths as wide as 1800 km with a resolution of ~25 km and an accuracy of 0.2 dB for 3σ [13]. To observe the FIZ, QS satellite data were used in the sea ice classification algorithm developed by Nghiem et al. [12]. Their results revealed a band of circumpolar FIZ containing older and rougher sea ice in the zone adjacent to the sea ice edge, surrounding the internal sea ice pack consisting of younger and smoother sea ice. QS results in 2008 and on 22 September for each year in 1999-2009 identified the persistent existence of the FIZ [12].

We now use QS data in 2009 to observe how the FIZ evolves during the sea ice growth season from May through the peak sea ice extent in September (Figure 1). The ice classes include rough older sea ice (RI), older sea ice (OI), younger sea ice (YI), melt on sea ice, and permanent ice as defined in the published literature [12]. Results in Figure 1 confirmed that the circumpolar FIZ, composed of RI and OI, had already formed by May in 2009. Encapsulating YI in the internal sea ice pack around Antarctica, the presence of the FIZ was persistent throughout the sea ice growth season as the ice cover expanded and reached its largest extent in September 2009. In particular along the longitude of 3.38°,
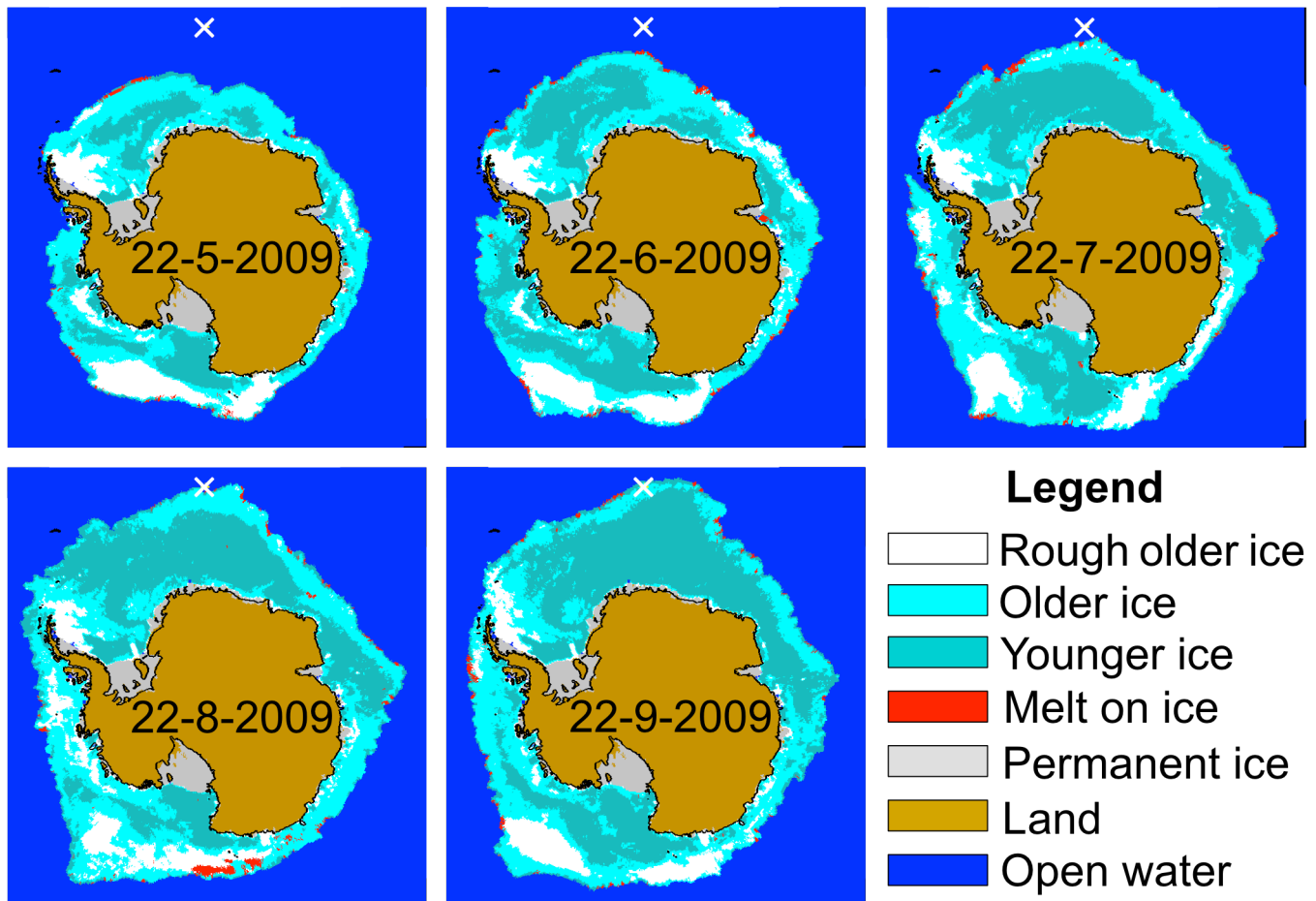
Figure 1. Antarctic synoptic sea ice classes throughout the ice growth season in 2009 observed by QS satellite data. Bouvet Island is marked by white cross.

sea ice advanced northward away from Antarctica to reach around Bouvet Island in August and could not extend much farther north in September 2009. The constraint of the sea ice edge near Bouvet Island is a recurrent feature also found in other years in 1999-2008 [12].

During the 2009 seasonal evolution of the Antarctic sea ice cover, the FIZ advanced outward in the circumpolar zone adjacent to the sea ice edge while the areal extent of the internal YI enlarged (Figure 1). This was due to persistent winds shaped by the Antarctic continental topography [12], forcing the transport of the internally produced YI outward to supply sea ice that continually built up and reinforced the FIZ along its south side. Some minor zonal areas of transient melt occurred on the surface of sea ice at different times in various locations near the sea ice edge (Figure 1).

III. OPERATION ICEBRIDGE MEASUREMENTS

Measurements from the OiB can provide relevant data to characterize the FIZ in more detail. The OiB is a NASA mission using aircraft to survey the Earth's polar ice to obtain three-dimensional view of Arctic and Antarctic ice sheets, ice shelves, and sea ice [14]. OiB flights have been conducted in September-November over various Antarctic locations in multiple years. We use OiB data acquired along the 3600-km Seelye Loop over the Weddell Sea in 2009 by

the Airborne Topographic Mapper (ATM) and by the Digital Mapping System (DMS). ATM is a scanning laser altimeter developed at the NASA Wallops Flight Facility in Virginia, and DMS is an airborne digital high-resolution camera maintained and operated by the Airborne Sensor Facility at the NASA Ames Research Center in California.

ATM measurements include surface elevation, slope, and roughness [15] with a sample width of 80 m and a pacing of 40 m on the surface along the flight track. Figure 2 presents ATM roughness along the OiB Seelye Loop flight on 24 October 2009, overlaid on a QS map of synoptic sea ice classes on the same day for comparison. The ATM roughness data have been averaged in each bin of $0.25^o \times 0.25^o$ in latitude and longitude along the OiB flight line. Overall, ATM observations show the largest roughness on RI, medium roughness on OI, and smaller roughness on YI. This is consistent with the general characteristics of the synoptic sea ice classes [12]. However, there is some discrepancy due to a mismatch in the spatial resolution of ATM and QS data to be cautioned in the comparison.

DMS data are processed to obtain geolocated and orthorectified images that represent the surface topography or digital elevation model (DEM). DMS DEM has a relative accuracy of ~0.2 m and a resolution of 10 cm × 10 cm [16] over a swath width of several hundred meters depending on
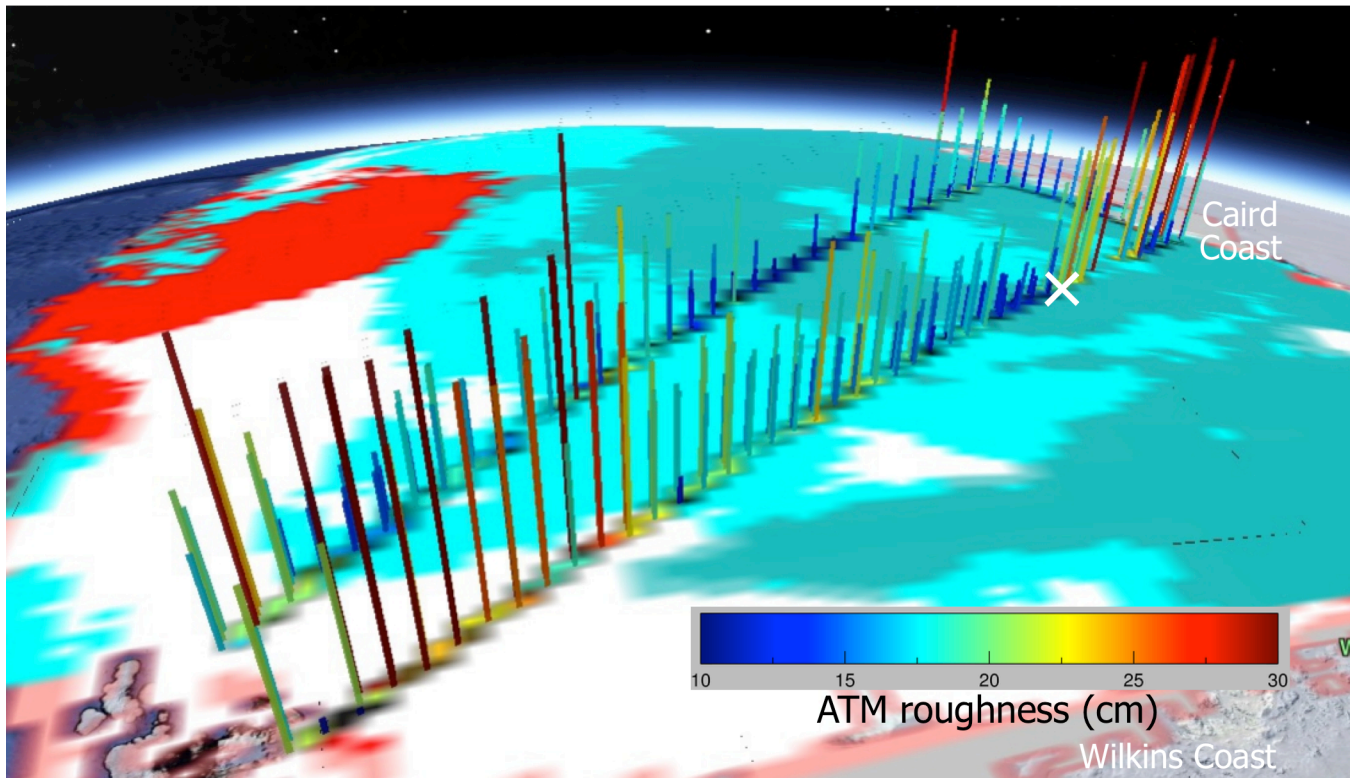
Figure 2. ATM measurement of sea ice surface roughness along the 3600-km Seelye Loop flight on 24 October 2009 during the NASA Operation IceBridge campaign over the Weddell Sea, together with QS sea ice classes on the same day. The white cross marks the location of the DMS DEM strip in Figure 3.
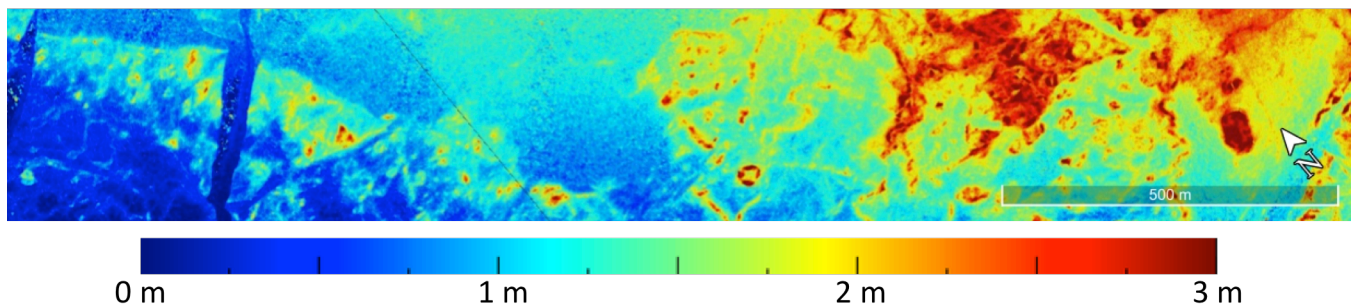

Figure 3. DMS measurement of snow-covered sea ice surface DEM in the Weddell Sea on 24 October 2009 during the Operation IceBridge campaign at the location marked by the white cross in Figure 2. The gray inset bar is a 500-m scale. This DEM is referenced to the minimum level of 0 meter.

the flight altitude. Within the DMS DEM accuracy limit, areas with pronounced features on sea ice surface such as deformed sea ice, ruble ice, pressure ridges, and other large-scale roughness [17] can be identified and statistically categorized over various sea ice classes. A 2-km segment of DMS DEM reveals a complicated surface of snow-covered sea ice varying over a range of more than 3 m (Figure 3).

IV.   DISCUSSIONS

The characteristics of the Antarctic circumpolar FIZ consisting of formidable sea ice are directly opposite to the feeble ice conditions in the marginal ice zone (MIZ) consisting of young and thin ice along the edge of the Arctic sea ice cover. As presented, the FIZ consists of older sea ice grown earlier in the sea ice season and gradually advanced outward away from the Antarctic coast.   The FIZ is continually built up by a supply of ice from the internal YI that can grow efficiently with a high growth rate, while the FIZ is furthermore sustained by a recirculation driven by persistent westerly winds and currents [12]. As observed in Figure 2, the FIZ has a larger roughness, corresponding a larger thickness as Toyota et al. [18] demonstrate that the mean ice thickness of Antarctic sea ice correlates with the surface roughness even better than with the mean freeboard. Persistently consisting of thicker ice, the circumpolar FIZ serves as a shield to protect the Antarctic sea ice cover. This is in a stark contrast to the Arctic MIZ that is easily reduced by melt and by wind and wave effects, making Arctic sea ice vulnerable to climate change. QS satellite scatterometer data acquired in 1999-2009, Oceansat-2 collected in 2009-2014, and SCATSAT-1 to be obtained in 2016-2021 together provide interdecadal observations of sea ice change.
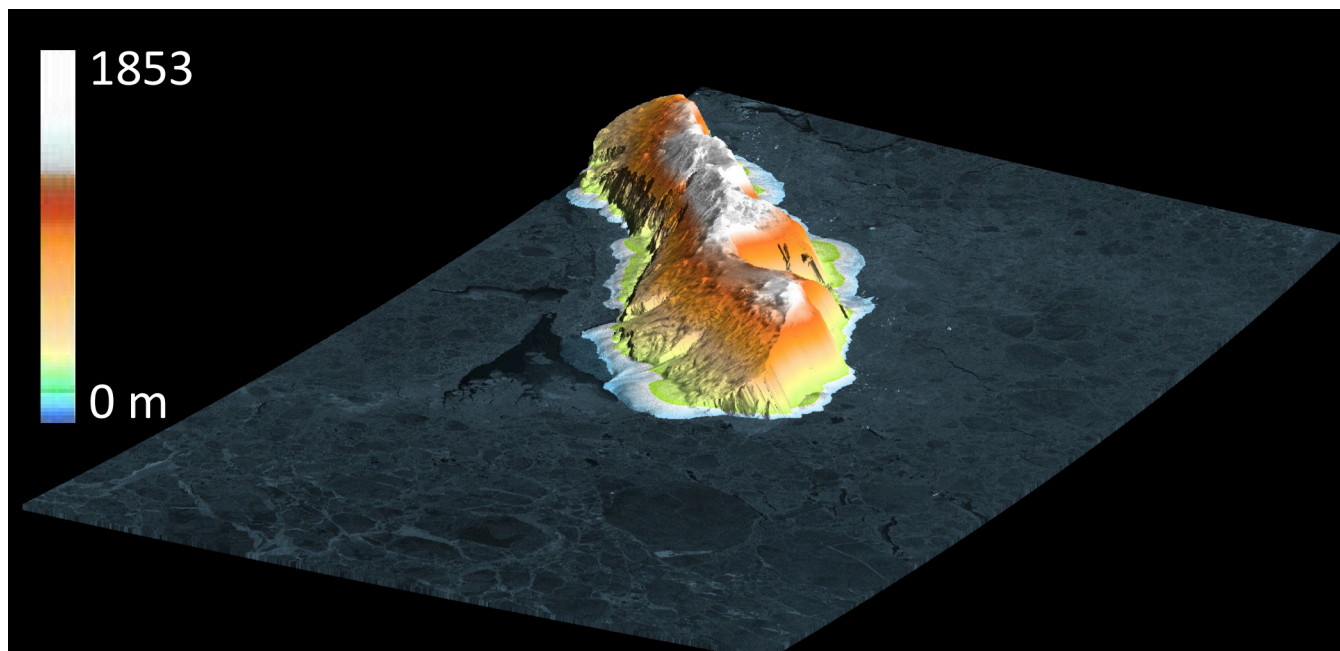
Figure 4. Example of TanDEM-X 2D backscatter pattern of Antarctic sea ice surrounding Sturge Island, located at 67.42°S and 164.73°E, where the island topography is measured in 3D by TanDEM-X interferometry.

To fully quantify the properties of the FIZ and to determine its long-term change demand extensive observations from the surface to aircraft and satellite levels at multiple scales in time and in space across the vast extent of the Southern Ocean over decades. This is particularly important to advance Antarctic science research, as there have been overwhelmingly more observations and modeling activities for the Arctic. A potential approach is to maximize the science return from the NASA's significant investment in the current OiB by developing a collaborative coordination with a future acquisition of a massive satellite SAR dataset, such as TanDEM-X [19] acquired over the Antarctic sea ice cover at its seasonal maximum extent, typically reached in the month of September or October.

The conceptual science plan is to conduct multi-phase surveys to obtain contemporaneous and collocated OiB and TanDEM-X data in conjunction with surface measurements using buoys, stations, and field observations from Antarctic icebreaker expeditions and drone operations. OiB ATM data can be used to calibrate DMS DEM, and then to compare with and correctly interpret TanDEM-X data in two (2D) and three dimensions (3D). While OiB can provide accurate and high-resolution measurements, the aircraft data are limited to a finite number of flight lines with pointwise or narrow-strip measurements. Once verified with OiB results, TanDEM-X can provide multiple measurements of sea ice properties across the vast coverage over Antarctic sea ice at its maximum extent, which may take more than 55 days to complete the massive TanDEM-X SAR data acquisition.

A major advantage is that the TanDEM-X SAR has monostatic, bistatic, polarimetric, and single-pass interferometric capabilities for robust ice and open water identification [20], sea ice classification [21], ice drift measurement [22][23], and DEM assessment [23] at a high resolution. For instance, open water detected by TanDEM-X is a crucial reference to estimate the sea ice freeboard from collocated OiB data. Since radar backscatter is sensitive to sea ice roughness [12] that correlates with sea ice thickness [18], TanDEM-X 2D SAR backscatter patterns are an independent source of information to cross-verify 3D DEM results from remote sensing estimates.   Then, the 2D SAR backscatter can be used to examine the spatial distribution of roughness and thickness of Antarctic sea ice. As DEM derived from SAR interferometry represents scattering center height, which is dependent on the penetration depth in snow-covered sea ice as a function of the electromagnetic wave frequency, DEM of the snow surface from coordinated OiB DMS optical data is necessary to understand and interpret TanDEM-X 3D observations over different sea ice classes that can be mapped in 2D by TanDEM-X data [21]. Moreover, the coordinated OiB/TanDEM-X Antarctic Science Campaign (OTASC) can be extended from sea ice into land to assess the DEM over terrestrial snow-covered ice, where the topography can shape wind patterns that exert a significant control on sea ice formation and evolution [12]. Figure 4 gives an example of TanDEM-X 2D and 3D observations of Antarctic sea ice surrounding Sturge Island to illustrate the versatility of the TanDEM-X capabilities.

Moreover, a fully polarimetric interferometry theory for bistatic radars [24], inherently reduced to the case of monostatic radars as a special case, has been derived based on the fundamental basis of the first principle of Maxwell's equations to preserve the phase information that is imperative for the interpretation of TanDEM-X polarimetric and interferometric data. This is crucial as the foundation of electromagnetic physics for 2D and 3D SAR signatures of snow-covered sea ice and land ice to develop remote sensing algorithms, considering noise effects at various resolutions

specifically required by different science research objectives. Results from aircraft and satellite algorithms can then be validated by surface truth and observations collected during Antarctic field campaign expeditions coordinated with remote sensing overflights.

The international community report on Global Satellite Observation Requirements for Floating Ice – Focusing on Synthetic Aperture Radar, specifically calls for the use of TanDEM-X capabilities to observe sea ice [25] in the Strategic Plan 2015-2018 of the Polar Space Task Group operated under the auspices of the World Meteorological Organization Executive Council Panel of Experts on Polar and High Mountain Observations, Research, and Services [26]. In view of multiple satellite missions for Earth science, results from the OiB/TanDEM-X coordinated campaign can serve as a reference to compare with results from future satellite missions such as the NISAR mission [27], the ICESat-2 mission [28], and the proposed Tandem-L mission [29]. From these missions, long-term validated remote sensing observations will be crucial as input to as well as verification of models for Antarctic sea ice seasonal prediction and decadal projection.

V. Summary and Conclusion

The Antarctic circumpolar FIZ is examined in this paper. Observations from remote sensing data show that the FIZ forms with sea ice produced earlier in the ice-growth season. Then the FIZ becomes older, rougher, and thicker as the Antarctic sea ice extent reaches its seasonal maximum in the austral winter-spring transition. In contrast to the feeble MIZ in the Arctic, the persistent FIZ encapsulates and protects the younger and thinner ice in the internal ice cover, and thereby contributes to the maintenance of Antarctic sea ice. The future OTASC field campaign is formulated to characterize the FIZ quantitatively, and to obtain a basic reference for comparisons with observations from future satellite missions to determine interdecadal change of Antarctic sea ice.

References

[1] J. E. Walsh, "A comparison of Arctic and Antarctic climate change, present and future," Antarctic Science, vol. 21, pp. 179–188, Jun. 2009, doi:10.1017/S0954102009001874.

[2] J. P. Liu and J. A. Curry, "Resolving the Paradox of Antarctic Sea-Ice Growth," Bull. Amer. Meteorolog. Soc., vol. 92, pp. 1411–1412, Nov. 2011.

[3] T. Maksym, S. E. Stammerjohn, S. Ackley, and R. Massom, "Antarctic Sea Ice-A Polar Opposite?" Oceanography, vol. 25, pp. 140–151, Sep. 2012.

[4] J. King, "A resolution of the Antarctic paradox," Nature, vol. 505, pp. 491–492, Jan. 2014.

[5] G. J. Marshall, "Trends in the southern annular mode from observations and reanalyses," Journal of Climate, vol. 16, pp. 4134–4143, Dec. 2003, doi:10.1175/1520-0442(2003)016<4134:TITSAM>2.0.CO;2.

[6] S.-W. Son et al., "Impact of stratospheric ozone on Southern Hemisphere circulation change: A multimodel assessment," J. Geophys. Res., vol. 115, 18 pp., Feb. 2010, doi:10.1029/2010JD014271.

[7] M. Sigmond and J. C. Fyfe, "Has the ozone hole contributed to increased Antarctic sea ice extent?" Geophys. Res. Lett., vol. 37, 5 pp., Sep. 2010, doi:10.1029/ 2010GL044301.

[8] S. Manabe, R. J. Stouffer, M. J. Spelman, and K. Bryan, "Transient responses of a coupled ocean-atmosphere model to gradual change of atmospheric CO_2. Part I: An- nual Mean Response," J. Clim., vol. 4, pp. 785–818, Aug. 1991, doi: 10.1175/1520-0442(1991)004<0785:TROACO>2.0.CO;2.

[9] J. Zhang, "Increasing Antarctic sea ice under warming atmospheric and oceanic conditions," J. Clim., vol. 20, pp. 2515–2529, Jun. 2007, doi: 10.1175/JCLI4136.1

[10] P. R. Holland, "The seasonality of Antarctic sea ice trends," Geophys. Res. Lett., vol. 41, pp. 4230–4237., Jun. 2014, doi: 10.1002/2014GL060172.

[11] J. Zhang, "Modeling the impact of wind intensification on Antarctic sea ice volume," J. Clim., vol. 27, pp. 202–214, Jan. 2014, doi:10.1175/JCLI-D-12-00139.1.

[12] S. V. Nghiem, I. G. Rigor, P. Clemente-Colón, G. Neumann, and P. P. Li, "Geophysical constraints on the Antarctic sea ice cover," Remote Sens. Environ., vol. 181, pp. 281-292, Aug. 2016, doi: 10.1016/j.rse.2016.04.005.

[13] W.-Y. Tsai et al., "Polarimetric scatterometry: A promising technique for improving ocean surace wind measurements," IEEE Trans. Geosci. Remote Sens., vol. 38, pp. 1903–1921, Aug. 2002, doi: 10.1109/36.851773.

[14] NASA. IceBridge Mission Overview. Available online from: https://www.nasa.gov/mission_pages/icebridge/mission/index .html, accessed Feb. 2017.

[15] W. B. Krabill. IceBridge ATM L2 Icessn Elevation, Slope, and Roughness, Vers. 2, Boulder, CO, USA: NASA DAAC at the National Snow and Ice Data Center, updated 2016, doi:10.5067/CPRXXK3F39RV, accessed Feb. 2017.

[16] R. Dominguez. IceBridge DMS L1B Geolocated and Orthorectified Images, Vers. 1, Boulder, CO, USA: NASA DAAC at the National Snow and Ice Data Center, updated 2016, doi:10.5067/OZ6VNOPMPRJ0, accessed Feb. 2017.

[17] Jet Propulsion Laboratory. Study Helps Explain Sea Ice Differences at Earth's Poles. Available online from: http://www.jpl.nasa.gov/images/earth/antarctica/20160520/P A121166.jpg, accessed Feb. 2017.

[18] T. Toyota, R. Massom, K. Tateyama, T. Tamura, and A. Fraser, "Properties of snow overlying the sea ice off East Antarctica in late winter, 2007," Deep Sea Research, Part II, vol. 58, pp. 1137–1148, May 2011, doi:10.1016/j.dsr2. 2010.12.002.

[19] DLR. TanDEM-X - the Earth in three dimensions. Available online from: http://www.dlr.de/dlr/en/desktopdefault.aspx/ tabid-10378/566_read-426/#/gallery/345, accessed Feb. 2017.

[20] L. Eriksson, G. Carvajal, A. Berg, L. Axell, and M. Johansson, "TanDEM-X measurements of sea ice drift and

sea surface current in the Fram Strait and in the Baltic Sea," *4th TanDEM-X Science Meeting*, DLR Oberpfaffenhofen, Germany, Jun. 2013.

[21] R. Ressel and S. Singha, "Comparing Near Coincident Space Borne C and X Band Fully Polarimetric SAR Data for Arctic Sea Ice Classification," Remote Sensing, vol. 8, 27 pp., Feb. 2016, doi:10.3390/rs8030198.

[22] I. Hajnsek et al., "TanDEM-X: First Scientific Experiments during the Commissioning Phase," *8th Euro. Conf. on Synthetic Aperture Radar*, Aachen, Germany, pp. 1–3, Jun. 2010.

[23] O. Lang, "TerraSAR and TanDEM-X Ice Information Products," *13th Meeting of the International Ice Charting Working Group*, Tromsø, Norway, Oct. 2012.

[24] S. V. Nghiem and J. J. Van Zyl, "Polarinetric Interfoerometry Theory," Manuscript, 25 pp., Jet Propulsion Lab, California Institute of Technology, Pasadena, Calif., USA, Jun. 2013.

[25] J. C. Falkingham et al., *Global Satellite Observation Requirements for Floating Ice – Focusing on Synthetic Aperture Radar*, 71 pp., Env. Canada, Mar. 2014.

[26] Polar Space Task Group, *PSTG Strategic Plan: 2015-2018*, 13 pp., World Meteorological Organization, Nov. 2015.

[27] Jet Propulsion Laboratory. *NASA-ISRO SAR Mission (NISAR)*. Available online from: http://nisar.jpl.nasa.gov/, accessed Feb. 2017.

[28] Goddard Space Flight Center. *Ice, Cloud, and Land Elevation Satellite-2 (ICESat-2)*. Available on line from: http://icesat.gsfc.nasa.gov/icesat2/, accessed Feb. 2017.

[29] A. Moreira et al., "Tandem-L: A highly innovative bistatic SAR mission for global observation of dynamic processes on the Earth's surface," *IEEE Geoscience and Remote Sensing Magazine*, vol. 3, pp. 8–23, Jun. 2015, doi:10.1109/MGRS.2015.2437353.

Towards the Estimation of Tree Biomass Changes in the Sparse Subarctic Forests Using Stereo WorldView 3 Images and Historical Aerial Photographs

Benoît St-Onge and Simon Grandin

Department of Geography,
University of Quebec at Montreal (UQAM)
Montreal, Canada
e-mail: st-onge.benoit@uqam.ca

Abstract—Subarctic forests are open woodlands sparsely populated by small trees having narrow crowns. They cover, in Canada alone, an area of more than 2.5 million km^2. Spread between the 50th and 70th northern parallels, these forests fall within the regions that are experiencing some of the greatest climate change that will likely induce variations in forest biomass. These changes could go undocumented due to the high costs of data acquisition in such remote areas of Canada. Airborne surveys (photo or lidar) are logistically difficult, and conventional remote sensing based on 2D satellite images (e.g., Landsat) lacks accuracy. Our goals are therefore to use new very high resolution satellite stereo images (31 cm pixels) to reconstruct 3D models of subarctic forests, and use historical stereo aerial photos acquired since the 1950s to create similar 3D models representing the structure of these forests in the past. In this study, we have reconstructed a digital terrain model (DTM) using stereo measurements on WorldView 3 images of sparsely wooded areas. We then performed similar stereo measurements on the top of trees and calculated their height by subtracting DTM elevations. These height measurements were in good agreement with reference data, and can afterward be used to estimate tree biomass. Similar measurements will be performed on historical aerial photographs, and the tree biomass changes, as a function of tree height and number of trees, will be estimated.

Keywords- forest; subarctic; WorldView; height, biomass.

I. INTRODUCTION

Subarctic forests, more specifically the open canopy lichen woodlands of the taiga ecoregions, cover more than 2.5 million km^2 in Canada alone, and occupy a good proportion of other northern nations, such as Russia. They are composed of sparse and rather short trees, and low species diversity (essentially, black spruces and dwarf birch). Roughly located between the 50th and 70th parallels, these environments will experience the greatest climate change. These generally include warming, but may involve an increase or decrease of precipitations. All these variations will likely induce changes in the forest height, density, productivity and species composition [1]. It can be hypothesized that, if growth is not limited by water availability, a significant rise in their productivity caused by the lengthening of the growing season and CO$_2$ fertilization will increase their biomass density (Mg ha^{-1}), and therefore their capacity to sequester carbon [2]. Such is the case for

example in the province of Quebec, Canada, where temperature and precipitation rose [3]. Few resources are however dedicated to the inventory of these vast forests, due to the high cost of airborne and field data acquisition in such remote areas, and because of their low commercial interest. This leaves us with very few precise data on the structure of these forests [4]. Using two-dimensional (2D) remote sensing methods [5], such as regressing forest height, density or biomass against the reflectance of Landsat images, or the backscattered microwave energy of spaceborne radars (e.g., ALOS/PALSAR), leads to prediction models having only moderate accuracy [6]. To calibrate the regression models, numerous field measurements need to be done within 1-2 years of image acquisition, in hardly accessible areas. This calibration is required for any new 2D image. Moreover, upcoming 3D satellite missions (circa 2020), such as BIOMASS (InSAR), or GEDI (lidar), will be on orbits that limit acquisition to 50° N, thus missing subarctic forests [7]. Airborne laser scanning (ALS) is extremely expensive to deploy in these regions because of remoteness, airport rarity, and the required very high laser point density [8]. Indeed, taiga trees are sparse and have very narrow crowns. Many go undetected by low-moderate density ALS because they fall in the gaps between zigzag-patterned laser scan lines [9]. Furthermore, we recently showed that when trees are sparse (discontinuous canopy), the estimation of height becomes ambiguous when using InSAR from TanDEM-X, precluding the use of this sensor for subarctic forests [10].

High resolution imagery (pixel size <=0.3 m) does not suffer from the problems of ALS (inter-scan line gaps) or InSAR (complex scattering behaviour in sparse forests). Stereo measurements performed on aerial images allow the accurate estimation of tree height when ground elevation data is available [11]. Recently, stereo-image acquisition from space, has significantly improved [12]. Notably, the WorldView-3 and 4 imaging sensors from Digital Globe, launched respectively in August 2014 and November 2016, offer an unprecedented resolution from space (0.31 m). They have stereo imaging capacities and their orbit covers the globe up to 80° N, thus encompassing all of the subarctic forests. The photogrammetric quality of WorldView 3 has been shown to be high [13]. Since subarctic forests are sparse, the ground is often visible between trees, thus

enabling the reconstruction of a digital terrain model (DTM) without the use of airborne lidar. If the apex of trees, typically narrow black spruces (*Picea Mariana*) in northern Canada, the height of single trees could be measured by stereo measurements performed on tree apices followed by subtraction of the ground elevation. Biomass of single trees can then be predicted using allometric equations. Repeating this operation for all visible trees over given plots then allows the calculation of biomass density. For areas where historical aerial photographs exist, the same operation can be performed, allowing the estimation of biomass change. As a first step towards these goals, we have assessed our capacity to estimate the height of single trees on a stereo-pair of WorldView 3 images in a sparse Canadian forest. The results were compared to the values extracted from an airborne lidar canopy height model (CHM). We have also verified if the manual procedure for measuring tree height could be automated by applying image matching techniques to the WorldView images to create a 3D point cloud.

We first explain the methods used for measuring tree heights on the WorldView stereopairs and how we compared these measurements to corresponding lidar heights (section II). In the following section, we present quantitative as well as image-based results. Finally, we discuss these results and provide an outlook of future research (section IV).

II. METHODS

A. Study region and data

Pending the acquisition of WorldView 3 or 4 imagery in true subarctic forests (planned for summer of 2017), we have used available data (imagery and lidar) in an area of the Canadian boreal forest centered at 49°54' N, 71° 34' W. The area has a gentle topography, and is populated mostly by black spruces growing in closed or open canopies. Sparsely wooded subareas were selected for this study.

A WorldView 3 stereo-pair acquired on June 6th 2015 in ortho-ready format, with rational polynomial coefficients (RPC), were used. View angles were respectively 12.7 and 24.3 degrees off-nadir, and sun elevation was 61.5 degrees at the time of acquisition. While nominal pixel size at nadir is 31 cm, the obliquity of the images caused this size to be slightly larger.

An airborne lidar CHM was retrieved from the province of Quebec's (Canada) open lidar archive. This data was captured in summer of 2013, and transformed to a 1 m resolution raster CHM by the provider. The initial lidar point clouds had a density of at least 2 points per m^2 (first or single returns). The 2D coregistration between the WorldView stereo-model and the lidar models was checked visually and found to be very good. The RPCs were therefore not adjusted.

B. Measurements

An interpreter performed stereo-measurements on the WorldView pair viewed in stereo using liquid crystal shutter glasses, and checked his pinpointing of tree tops using a monocular split screen strategy. The elevation of 30 tree apices were thus measured in 3D. For each tree, a similar measurement was made of ground elevation in the immediate vicinity of the tree. All stereo-measurements were performed using the Summit Evolution software application (DAT/EM Systems International, U.S.A.). The stereo height of trees (H_S) was computed by simply subtracting the ground elevation associated to the tree from the elevation of its apex. The lidar tree height (H_L) was extracted by reading the CHM value of the highest lidar pixel within each crown corresponding to the stereo measurements. The set of H_S and H_L values were compared by computing the bias (average of H_S - H_L), root mean square error (RMSE), and r^2. The ground elevations at the XY position where terrain level stereo measurements were made (GE_S) were compared to the elevations of the lidar DTM at these positions (GE_L). The set of GE_S and GE_L values were compared using the method used for H.

Three image matching algorithms were tested: Correlator 3D (Simactive, Canada), MapMatrix (VisionTek, China), and OrthoEngine (PCI Geomatics, Canada). The number of available matching algorithms is limited by the fact that solutions applicable to (pushbroom) WorldView imagery are still few, compared to those using (full frame) airborne imagery. In our trials, the 3D models produced by Correlator 3D were the best, so results are presented only for this algorithm. Subtracting the ground elevations of the lidar DTM from the surface elevations automatically extracted from the stereo WorldView images produced a stereo-lidar CHM (CHM_{SL}). Alternatively, low photogrammetric points within local neighborhoods were classified as ground points and interpolated into a stereo DTM (DTM_S). An entirely stereo-photogrammetric CHM (CHM_S) was generated by subtracting the WorldView surface points from the DTM_S. These models (CHM_{SL}, CHM_S) were each compared pixel-wise to the lidar CHM (CHM_L) using, again, bias, RMSE and r^2 (i.e. CHM_{SL} - CHM_L , CHM_S - CHM_L).

III. RESULTS

Figure 1 shows corresponding excerpts from each of the WorldView image forming the stereo-pair. In can be seen that individual trees can be well resolved, even in the case where trees are short and crowns are narrow.

H_S values ranged from 3.7 m to 14.7 m, with a standard deviation of 2.7 m. Compared to lidar, a bias of 0.19 m, a RMSE of 2.11 m, and a r^2 of 0.63 was obtained. Figure 2 presents a scatter plot of the H measurements. A clear outlier caused by a tree that was likely most entirely missed by lidar led to a +7.7 m difference (top-left data point in Figure 2). When this observation was removed, the bias and RMSE dropped to -0.07 m and 1.62 m respectively, and the r^2 increased to 0.77. In the case of ground level measurements, these values were respectively -0.73 m, 1.06 m, and 0.98.
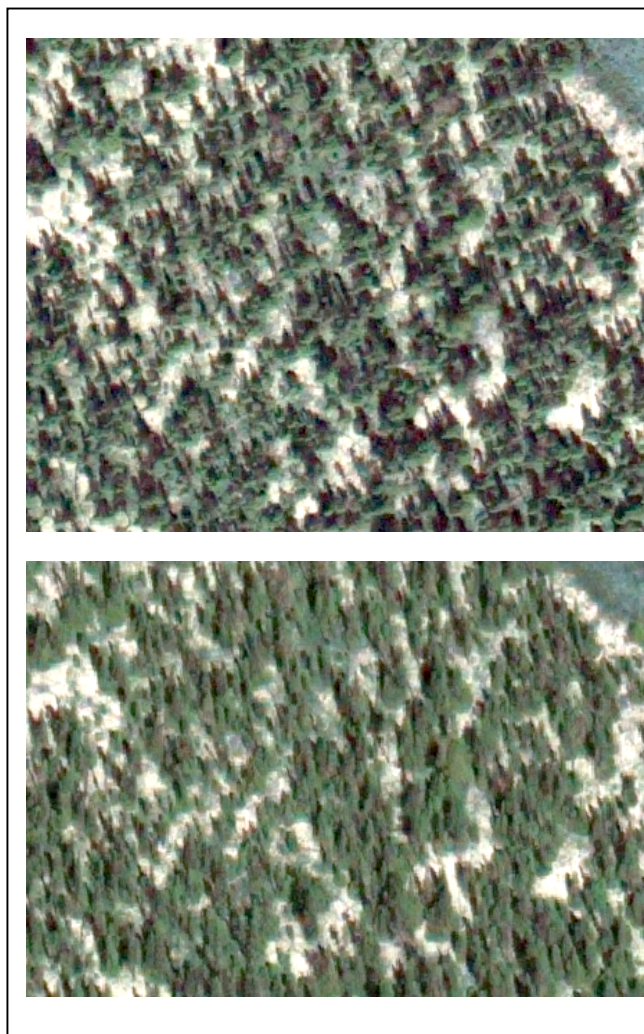
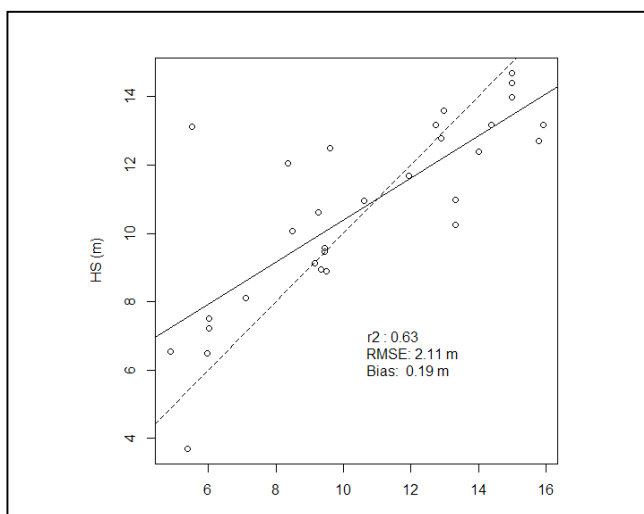Figure 1. Corresponding excerpts of the WorldView 3 stereo pair.

Figure 2. Scatterplot of the stereo (H_S) vs lidar tree heights (H_L).
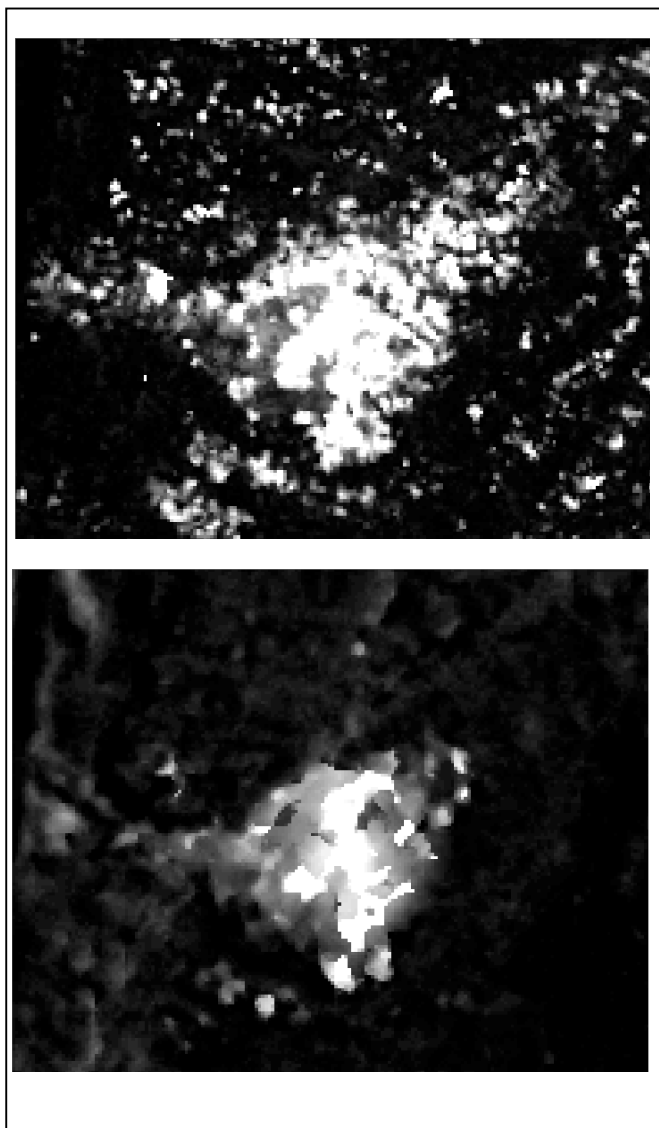

Figure 3. Lidar (top) and stereo CHM excerpts (unrelated to Figure 1).

Excerpts from the lidar and stereo-lidar CHMs appear in Figure 3. The CHM_{SL} is clearly lower and less resolved than the CHM_L. The bias, RMSE and r^2 between the different types of CHM are respectively, for CHM_{SL} - CHM_L, -0.51 m, 2.98 m, and 0.29, and for CHM_S - CHM_L, -1.2 m, 3.13 m, and 0.28.

IV. DISCUSSION AND CONCLUSION

The discrepancy between the H_S and H_L measurements must be interpreted with care. At this phase of our study, lidar was used as reference for tree height, despite shortcomings. The lidar point density was rather low for ensuring that the top of the narrow crowns be hit in such a way that they would have generated a return at an elevation close to the tree apex. Furthermore, the rather large pixels size of the CHM (1 m) may have introduced more

uncertainty. In this context, it appears that the manual measurements are quite accurate (conservative estimate of RMSE = 1.62 m). In general, we may expect the height measurement to be slightly underestimated, both in the stereo and lidar measurements. The presence of shrubs on the ground may have elevated the perceived terrain level, while lack of resolution of the apex of the crown may have diminished the top elevation. The larger ground level bias, at -0.73 m, accompanied with a lower RMSE (1.06 m) suggests that there might have remained a slight Z misregistration (negative bias) but that stereo measurements are actually very precise when the object is easily scannable by lidar (lower G_S - G_L RMSE).

Automating the creation of tree height data through stereo-matching will represent a significant challenge in light of the results we have presented. The coefficient of determination (r^2) did not exceed 0.29, while they reached 0.77 for manual measurements. This is not entirely surprising for these types of sparse forests. Because the trees do not form a closed carpet-like canopy, the surface to be reconstructed is very complex. It is formed by a smooth base layer (terrain) over which sharp isolated peaks (trees) protrude. In many circumstances, the side of a tree is visible in one image, and the opposite side in the other (Figure 1). Also, tree leaning caused by obliquity occurred in different directions. The relatively high level of obliquity of the stereo pair that we have used probably aggravated this situation. It seems unlikely that current image matching algorithms will be able to produce usable photogrammetric points clouds for subarctic forests before significant improvements are made to their matching strategies.

Nevertheless, we have shown that using a manual stereo measurement approach, the accuracy of the individual tree heights is at least 1.62 m. Once this is ascertained in a true subarctic forest using precise field measurements of tree height, it signifies that we could easily measure the height of single trees of any plot, however remote and inaccessible it may be. This method would probably not be applied wall-to-wall over the vast subarctic forests of the world on the short term due the high cost of the imagery. However, it can be used as a dense sampling tool across large regions. This would greatly enhance our capacity to create new knowledge on the current state of these forests. Time series of these measurements, whether pastward using historical images, or forward by repeating similar measurements in the future, will allow a better understanding of the dynamics of height, density, and therefore biomass of sparse but vast subarctic forests.

REFERENCES

[1] G. S. Payette, M. J. Fortin, and I. Gamache, "The Subarctic Forest–Tundra: The Structure of a Biome in a Changing Climate", Bioscience, vol. 51, pp. 2301-2316, 2001.

[2] R. Poyatos et al, "Environmental and Vegetation Drivers of Seasonal CO2 Fluxes in a Sub-arctic Forest–Mire Ecotone, vol. 17, pp. 377–393, 2014.

[3] L. D'Orangeville et al. "Northeastern North America as a potential refugium for boreal forests in a warming climate". Science, vol. 352, pp.1452-1455, 2016.

[4] M. Wulder, C. Campbell, J. White, M. Flannigan and I. Campbell, "National circumstances in the international circumboreal community", For. Chron., vol. 83, pp. 539–556, 2007.

[5] A. Beaudoin, et al, "Mapping attributes of Canada's forests at moderate resolution through kNN and MODIS imagery" Can. J. For. Res., vol. 44, pp. 521–532, 2014.

[6] I. Olthof, and D. Pouliot, "Treeline vegetation composition and change in Canada's western Subarctic from AVHRR and canopy reflectance modeling" Remote Sens. Env., vol. 114, pp. 805–815, 2010.

[7] D. H. T. Minh et al, "Capabilities of BIOMASS Tomography for Investigating Tropical Forests" IEEE Trans. Geo. Rem. Sens., vol. 53, pp. 965–975, 2015.

[8] N. Thieme, O.M. Bollandsås, T. Gobakken and E. Naesset, "Detection of small single trees in the forest–tundra ecotone using height values from airborne laser scanning" , Can. J. Rem. Sens., vol. 37, pp. 264-274, 2011.

[9] N. Stumberg, M. Hauglin, O.M. Bollandsås, T. Gobakken and E. Naesset, "Improving Classification of Airborne Laser Scanning Echoes in the Forest-Tundra Ecotone Using Geostatistical and Statistical Measures", Rem. Sens., vol. 6, pp. 4582–4599, 2014.

[10] Y. Sadeghi, B. St-Onge, B. Leblon and M. Simard, "Canopy Height Model (CHM) Derived From a TanDEM-X InSAR DSM and an Airborne Lidar DTM in Boreal Forest", JSTARS, vol. 9, pp. 381 - 397, 2016.

[11] B. St-Onge, J. Jumelet, M. Cobello and C. Véga, "Measuring individual tree height using a combination of stereophotogrammetry and lidar". Can. J. For. Res., vol. 34, pp. 2122-2130, 2004.

[12] S. Gehrke K. Morin, M. Downey, N. Boehrer and T. Fuchs, "Semi-global matching, an alternative to lidar for DSM generation?". I. Arch. Phot. Rem. Sens. Spat. Inf. Sci., XXXVIII–B1, 1–6, 2008.

[13] F. Hu, X.M. Gao, G.Y. Li and M. Li, "DEM extraction from WorldView-3 stereo-images and accuracy evaluation", I. Arch. Phot. Rem. Sens. Spat. Inf. Sci., vol. XLI-B1, 23rd ISPRS congress, 2016. pp. 327-332.